Jupiter's Turbulent Power Spectra from Hubble Space Telescope

Richard G. Cosentino[a,b], Amy Simon[b], Raúl Morales-Juberías[c]

[a] *NASA Postdoctoral Program Fellow, NASA Goddard Space Flight Center, 8800 Greenbelt Rd, Greenbelt MD 20771 (U.S.A.)*
[b] *Solar System Exploration Div., NASA/GSFC, Greenbelt MD 20771 (U.S.A.)*
[c] *Physics Department, New Mexico Institute of Technology, Socorro NM 87801 (U.S.A.)*

Abstract

Turbulence in Jupiter's atmosphere was investigated with archival and ongoing observations from the Hubble Space Telescope (HST). Data sets that include one full rotation (360° longitude coverage) were used to produce complete maps of the planet's upper cloud layer. The global maps were analyzed to generate the passive tracer power spectrum of cloud features for single rotation observations. Successive rotations produced pairs of maps such that zonal winds and the zonal kinetic energy power spectra were calculated. An atmosphere's dimensionality and dynamics are reflected in the slopes of such turbulent power spectra. Many of the retrieved passive tracer power spectra have a shallow spectral index over wavenumbers $k \sim 1 - 30$ and transition to the well-known Kolmogorov $k^{-5/3}$ relation at smaller scales between wavenumbers $k \sim 30 - 1000$. The transition scale is similar to the number of jets in Jupiter's zonal wind profile and is related to the Rhines scale and the beta effect induced anisotropy scale. We also report on differences found in anti-cyclonic and cyclonic shear region power spectra and how they correlate to latitudinal changes in the zonal wind profile. We found that properties of Jupiter's power spectra are consistent with quasi-geostrophic turbulence for shallow fluids.

Keywords: JUPITER, TURBULENCE, POWER SPECTRA,

1. Introduction

Understanding the dynamics of an outer planet's atmosphere ultimately adds to our understanding of the entire planet. Recent studies have analyzed how the east-west or zonal winds on Jupiter temporally evolve and spatially vary [38, 43, 22]. Jupiter's zonal wind profile is very stable with only a few locations experiencing significant changes in velocity with time, such as jet near 24°N. The continual banded appearance of light and dark clouds in Jupiter's atmosphere is occasionally disrupted by sporadic events that do not last very long [13]. At the smallest scales, we see storms rapidly evolve and local cloud features get sheared apart [10]. Turbulent processes at large and small scales interact

Email address: richard.cosentino@nasa.gov (Richard G. Cosentino)

with local chaotic and larger laminar flows creating and maintaining Jupiter's appearance when viewed from afar.

The upper cloud layer of Jupiter is affected by the dynamics of the unseen regions beneath it. The exact mechanisms and processes that dominate this connection are still poorly understood but are crucial to understanding the planet as a whole [16]. Some models suggest that the upper cloud layers of Jupiter are connected via cylinders extending through the planet, so that the winds in the upper clouds are the same as those at greater depths [5]. Alternative models suggest that coupling could be weak via deep convection, and so the winds at depth do not necessarily resemble the observed winds in the cloud deck [19]. The Galileo probe measured winds in a strong eastward jet that approached a constant speed over a pressure range of 4-20 bars [1, 46] but there is no clear consensus that the same vertical wind profile is applicable globally [21].

Optical images of Jupiter capture snapshots of the turbulent behavior of the ammonia ice clouds with a pressure base near 0.7 bars [28, 11, 10]. High resolution ($\sim$0.1°) maps produced from HST observations, like that shown in Figure 1, display fine structures in the upper cloud deck, such as small-scale storms, eddies, waves and of course, turbulent, non-laminar flow [20, 17, 39, 36]. Many features resemble those seen in the Earth's atmosphere, where they are primarily driven by convective processes. A similar origin is almost certainly true for Jupiter's atmosphere where there is evidence of lightning and scant water ice detections [30, 17, 37, 25, 4].

We can explore the regions underneath the clouds utilizing longer wavelength observatories like the National Radio Astronomy Observatory (NRAO) Very Large Array (VLA) [12, 9] or space based missions like Juno [3, 23]. In this paper, we studied these regions indirectly by analyzing global maps of Jupiter's atmosphere at optical wavelengths probing the cloud deck. Energy injected into an atmosphere is transferred and dissipated over a range of spatial scales. The spatial frequency distribution of features in the clouds or variations in the winds are predicted to obey spectral power law relations that depend mostly on the energy flux over these scales and the dimensionality of the atmosphere. Long-term observing programs offer the opportunity to study the turbulent behavior of Jupiter and create a deeper record of its atmospheric behavior in time. By analyzing a collection of power spectra, we could potentially connect the deeper regions of Jupiter to its upper cloud layers.

1.1. Turbulent Power Theory

The dynamics of Jupiter's turbulent cloud layer can be studied with observational maps and creating a power spectrum versus spatial frequency or wavenumber. The longitudinal wavenumber k is defined as the number of complete sinusoids that can fit in the circumference of the planet at a particular latitude. The meridional wavenumber n is similar but in the latitudinal direction. One power spectrum focuses on the motion of the clouds (kinetic energy) and the other examines the structure in the clouds (passive tracer). The kinetic energy power and residual spectra require 2-D wind fields to be calculated, where

as the zonal mean zonal kinetic energy power spectrum can generated from the 1-D zonal wind profile from observations with successive rotations. These last spectra will be the focus of a follow-up study.

A power spectrum for an atmosphere is calculated by performing a Fast Fourier Transform (FFT) on some type of signal amplitude. The passive tracer power spectrum "signal" is intensity fluctuations of cloud reflectivity as a function of longitude. The power spectrum can then be computed on a line-by-line basis over a range of latitudes to span particular areas of interest of the atmosphere. The complex response of the FFT is summed in Fourier space over all desired latitude points, and multiplied by its complex conjugate to acquire the complex amplitude. The kinetic energy power spectrum is generated from the sum of the squared zonal and meridional winds versus k, while the passive tracer power spectrum uses the spatial frequency of features as a function of k [45]. The kinetic energy power spectra are found by squaring the complex amplitude of the winds in either the zonal (k) or meridional direction (n).

The properties of a power spectrum indicate the dimensionality of the atmospheric region of interest, which also is related to the flow of energy or enstrophy between different physical scales; small to large or large to small [24]. The dimensionality of Jupiter's atmospheric dynamics, whether "shallow" or "deep", is an area of current research. A 3-D turbulent signature would suggest that the winds at the cloud layer are connected to the winds deeper down [5], but a 2-D signature might suggest the opposite, that the winds at the cloud layer are shallow and not strongly coupled to the dynamics of the deeper planet [19]. As new data are being acquired from the Juno mission, these theories may be required to be revisited [3, 29, 23].

Kolmogorov theory predicts an atmosphere in a 3-D turbulent regime should have a passive tracer power spectrum with spectral indices of $k^{-5/3}$ for increasing k, which is generated from the transfer of energy from large scales to small scales or low to high wavenumbers [32, 45]. A single change in the spectral slope will occur at a characteristic wavenumber k_d, where dissipative effects dominate energy losses; for wavenumbers greater than k_d, the passive tracer power spectrum will have a slope following a relationship of k^{-1}. Figure 2 shows the theoretical passive tracer and kinetic energy power spectra in the lower portion of the panel (a) for the 3-D case [27, 26].

In a 2-D turbulent regime with forcing at some characteristic size, a forcing scale at wavenumber k_f, there is a similar $k^{-5/3}$ relation for wavenumbers within an inertial subrange less than k_f. In the 2-D case however, energy is being injected into the atmosphere at k_f and an inverse energy cascade exists from high to low wavenumbers, smaller to large scale features and there is a "kink" or transition in the spectral index at this wavenumber. The passive tracer power spectrum for wavenumbers greater than k_f follows a k^{-1} relation. The kinetic energy power spectrum follows a k^{-3} relation between k_f and k_d where enstrophy cascades from the forcing scale to smaller scales, and further on to significant energy dissipation following k^{-n} with $n > 3$ for higher wavenumbers. Figure 2 shows the theoretical power spectra for a 2-D turbulent atmosphere near the top of the plot in panel (a).

Figure 2 panel (a) also shows estimated zonal wavenumber ranges for three dynamical scales; the Rhines scale (RS), the Rossby radius of deformation (RR), and a convective storm (GS). The Rhines scale has been estimated in the range of 6000-15,000 km for Jupiter [15, 31] and physically corresponds to the width of a jet and the size at which the inverse energy cascade could stop [33, 40]. The Rossby radius was estimated to be around 1200-2900 km for latitudes between $20 - 40°$ [47], while Gierasch et al. [17] estimated the size of moist convective storms on Jupiter to be around ∼1000 km or larger. Both the Rossby radius and moist convective storms could represent the a forcing scale k_f according to theory if the forcing mechanism is driven by baroclinic instabilities [6] or latent heat release in moist convection [17], respectively. Different scales, such as the beta scale, can be estimated from analysis of kinetic energy power spectra and will be compared to results of this research in a future study [44, 42, 15].

While the theory for turbulent power spectra has been around for many years and some observations point towards the theory's accuracy, other observations indicate it is still incomplete. Determining to what extent an atmosphere like Jupiter is dominated by quasi-geostrophic turbulence, which is more 2-D like than 3-D like, can aid in our understanding of the flow of energy in the entire planet. Because the $k^{-5/3}$ relation appears over a range of different scales for different turbulent regimes, we had to be cautious in determining the significance of the results we found. These points were kept in mind as we began our analysis of the data contained in the HST observations, being cautious not to introduce any artificial bias towards trying to find any $k^{-5/3}$ or k^{-3} relations expected from theory.

1.2. Relevant Background

Previous studies of Jupiter's turbulent power spectra that are referenced several times within this work are now presented for background context to compare our techniques and results. An early study conducted by Harrington et al. [18] analyzed infrared maps generated from $4.9\mu m$ emission observations to determine the power spectrum of Jupiter between $\sim 2 - 4$ bars of pressure. They manually determined a break in the power spectrum near $k \sim 26$ and fit eastward and westward jets spectra with power laws over the wavenumber ranges $k = 1 - 24$ and $k = 28 - 60$. Harrington et al. [18] found a -0.7 slope for both jet directions in the low wavenumber range and found approximate slopes of -2.7 and -3.1 for eastward and westward jets, respectively. Their observations sometimes had gaps and resulted in some partial maps that required Harrington et al. [18] to use a Lomb-normalization instead of FFT analyses when deriving spectral power. The validity of this substitution was not fully explored but preliminary explorations we conducted on synthetic spectra concluded that there is no impact on the transition wavenumber. However, spectral indices, especially at higher wavenumber ranges, found with a Lomb-Scargle approach were approximately double the true spectral index of the synthetic spectrum.

Two commonly referenced citations in our work are Barrado-Izagirre et al. [2] and Choi & Showman [7], who both used optical maps generated from HST or the Cassini mission flyby to analyze power spectra. They both developed

similar automated approaches to find a "kink" or break in the spectral slopes between low and high wavenumbers, treating the location of that break as a free parameter. To remove the effects of large scale waves, like the planetary Rossby wave near 8°N, both started their spectral fitting at a low wavenumber of $k = 10$. Barrado-Izagirre et al. [2] found a range of low wavenumber spectral slopes between [-1.1,-1.6], and a spectral index for higher wavenumbers between [-2.0,-3.1] with transitions around $k \sim 80$; we will call these slopes m_1 and m_2. Choi & Showman [7] found m_1 slopes between [-1.3,-1.8] and m_2 slopes between [-2,-3] with transitions between $k \sim 67 - 300$. We exclude results from haze analyses because we did not conduct it in our research.

Cosentino et al. [9] investigated the power spectrum from long wavelength observations sensing between 1-2 bars of pressure with the VLA at radio wavelengths of 2 cm. Analysis of their map's power spectrum using an automated approach found a break at a wavenumber near $k \sim 28$, which is similar to Harrington et al. [18]. Cosentino et al. [9] had a low wavenumber constraint of $k = 5$ due to interferometry observational and synthesis effects and found spectral indices of -1.6 and -1.0 for m_1 and m_2, respectively.

Young & Read [47] used several consecutive Cassini flyby maps to derive 2-D winds and the kinetic energy power spectrum. They manually determined a transition in their power spectrum near $k \sim 26$. They found a spectral slope for m_1 at low wavenumbers of -0.7, while the high wavenumber spectral slope m_2 was near the well known Kolmogorov relation of $k^{-5/3}$.

This study incorporated techniques and results from these previous studies. We used a wavelength that probes the upper cloud deck from HST observations spanning 1995-2017, Section 2. In section 3 we describe how we calculated the spectral slopes, leaving the transition between them as a free parameter by calculating the spectral slopes, leaving the transition between them as a free parameter [2, 7, 9]. We did not impose a low wavenumber limit to start spectral fits, starting at k = 1 [18, 47]. Finally, in section 4, we compare the spectral power properties at different latitudes and within different shear regions of the atmosphere.

2. Observations

We compiled HST observations of Jupiter from 1995-2017 in 4 different filters that were included in our analysis as presented in Table 1 to investigate the passive tracer power spectrum. The filter wavelengths (631 nm, 673 nm, 763 nm, and 953 nm) were chosen because they contained the least amount of scattering from hazes and are most sensitive to cloud structure in the uppermost cloud layer [38]. Only observations that spanned all longitudes of Jupiter were projected onto a cylindrical surface to produce a cartographic representation of the planet. The maps use planetographic latitudes (used throughout this paper) and are similar to the popular Mercator projection for Earth maps. An example of a map is shown on the left side of Figure 1 at the filter wavelength of 631 nm which was generated as part of the Outer Planet Atmospheric Legacy (OPAL) program [36].

The maps are generated by stitching together images from consecutive HST orbits to cover all longitudes of the planet as it rotated. Full global maps require 5-6 HST orbits to span Jupiter's full 10-hour rotation. Some observations were planned to map complete successive rotations of Jupiter to allow wind measurements (e.g., Tollefson et al., 2017; Johnson et al., 2018). To make a complete map, individual images are navigated with iterative ellipsoid limb fitting and mapped at 0.1°/pixel over ±79.8° of latitude and ±40° of longitude. Minnaert functions are applied to reduce limb effects, using empirical fits to the k coefficient, ranging from ∼0.5 to 0.999 at UV to near IR bands, respectively [36]. To generate a global map, individual maps are joined at overlapping longitudes, and seams are smoothed with a weighted average over ±1° at the map edges. The seams are most easily observed at high latitudes in filters that are sensitive to high altitude hazes above the cloud deck (UV and methane gas absorption band filters).

The right panel of Figure 1 displays the spectral power of the map as a function of latitude versus planetary wavenumber k. A thin vertical line marks $k = 6$ which shows significant spectral power at high latitudes. The map seams alter the power spectrum at wavenumbers $k = 6$ and $k = 7$ and so they, and their corresponding spectral power values were not included in our power spectrum fitting algorithm. This point will be discussed in detail later, but is noteworthy now since it is produced by the mapping process.

There are two other prominent spectral power features in the right panel of Figure 1 that warrant discussion now also. First, is the high amount of spectral power at $k = 1$ found at several latitudes. There are large scale variations in map intensity at latitudes near 30°N and between 10-15°S. Revivals in Jupiter's off-equatorial belts and large scale disturbances generate these typical "half" globe spanning brightness patterns which the FFT fits with a wavenumber $k = 1$. These features are quasi-periodic and almost sporadic, impacting the region's appearance quickly and evolving rapidly over relatively short time scales until finally reaching their more familiar state sooner than later [13]. Therefore, we do not consider events and features like these to be a dominant component of Jupiter's turbulent power spectrum, so the $k = 1$ wavenumber and power are ignored in our spectrum fitting algorithm as will be discussed later.

The second spectral power feature is related to the high power values found over a range of wavenumbers near the North Equatorial Belt's (NEB) southern boundary at 10°N. The spectral power concentrated at wavenumbers between $k = 8-12$ corresponds to the well-known "hotspots" wave feature in this region. Several studies have found similar spectral power peaks at these wavenumbers and are attributed to the long-lived planetary Rossby wave residing at this latitude [34, 14, 46, 8, 9].

Table 2 shows the Earth-Jupiter range, the focal length, equatorial resolution and calculated upper wavenumber limit for each observation in Table 1. The highest wavenumber limit (k_{max}) at the equator is given by:

$$k_{max} = \frac{\pi R_j}{\Delta x_{res}} \tag{1}$$

where Jupiter's equatorial radius is R_j=71,492 km and Δx_{res} is the native resolution element. Table 2 presents equatorial k_{max} values for two adjacent Δx_{res} elements to be natively resolved. The superscript "1" notes the observations with the highest equatorial resolutions and were additionally analyzed to sensitivity tests exploring different high wavenumber limits k_{high}=500, 1000 and 1500 (see Appendix). Older observations and those not near opposition did not undergo the same additional sensitivity tests.

We investigated the projection effects of higher latitudes on the wavenumber limits we could confidently resolve to determine their impact on both resolution and high wavenumber limits. We found that most of the observations taken using WFC3 at latitudes of ±40° could still well-resolve a k_{max} ∼1000, even when including projection effects of 30° off the central meridian in longitude. We extended these calculations up to ±60° in latitude and found that observations in Table 2 with the superscript "1" found the high wavenumber limit decrease to the range of k_{max}=883-916. These high wavenumber limits marginally decreased when including projections of 30° off the central meridian in longitude to the range of k_{max}=818-848. The Appendix shows the robustness of modeled power spectra fits from tests where varying values of k_{high}=500, 1000, and 1500 at equatorial latitudes had almost no impact on the derived fit parameters. Similarly, the same experiments on data sets that included a larger range of latitudes also produced very little variation in modeled power spectra fits.

3. Power Spectra Fitting

3.1. Passive Tracer Composite Model

Studies by Barrado-Izagirre et al. [2] and Choi & Showman [7] investigated turbulent power spectra derived from maps produced from selected optical wavelength HST and Cassini observations. They analyzed their power spectra with a composite model of two linear fits in log-log space of power versus wavenumber. The composite model had ranges of low and high wavenumber linear fits with power law slopes of m_1 and m_2, respectively. The transition between m_1 and m_2 was a free parameter, represented by the variable wavenumber k_T, which is the "kink" or "break" in the spectrum. We implemented a similar model of two line segments to fit the derived tracer power spectra for all observations in Table 1 and recorded the best fit values for m_1, m_2 and k_T where it minimized χ^2 of all possible fits. The transition wavenumber k_T can possibly represent the theoretical forcing scale, k_f discussed earlier, or could represent other dynamical scales which could alter the power spectrum by affecting the inverse energy cascade, such as the Rhines scale [33, 40].

Cosentino et al. [9] applied a similar algorithm to a radio emission map produced from the VLA probing fine-scale structures below the upper-cloud deck. They began exploring the limitations of such a composite model to sensitivity tests on parameters like the low wavenumber (k_{low}) and high wavenumber (k_{high}) limits to a power spectrum's fit. Barrado-Izagirre et al. [2] and Choi & Showman [7] set a lower wavenumber limit of k_{low} = 10, but they never

presented a full sensitivity study of their results to that parameter. The high wavenumber limit for Barrado-Izagirre et al. [2] and Choi & Showman [7] were $k_{high} = 150$ and $k_{high} = 1000$, respectively, and this parameter was also not subjected to sensitivity analysis in their studies. We decided to investigate the sensitivity of both parameters in our research.

While Barrado-Izagirre et al. [2], Choi & Showman [7], and Cosentino et al. [9] used similar composite models, a full investigation to applying such a model over the time span of observations that we analyzed had never been done before. Additional aspects not fully considered in previous studies, such as latitude domains, image contrast, the length of line segments, and convergence of fits with sensitivity to low wavenumbers, were for the first time investigated in this study. Details are presented in the next subsection (and the Appendix) where additional modifications, calculations, or considerations to results of the composite model algorithm were required.

3.2. Algorithm Details from Initial Findings

The length of linear segments of the model were varied and we found that an automated process sometimes bypassed a scientifically significant result that was found for convergent k_T values. A detailed explanation and example is included in the Appendix where we go through nuances of finding such a result at low wavenumbers, even though that result was not found to be the majority through an automated search. Though manual inspection of all of our results ultimately took much longer, we felt more confident in that process and only used automated reporting when deemed appropriate.

One such convergence we found through manual inspection was many models found $k_T = 6$ or $k_T = 7$ for low k_{mod} values. (The parameter k_{mod} is the minimal length of one of the line segments used to fit the power spectrum - see Appendix for details.) We attributed the excess power found in $k = 6$ and $k = 7$ to the previously mentioned seams in the maps. The large spectral power at these wavenumbers at high latitudes limited our map analyses to $\pm 60^\circ$ and lower latitudes. We ultimately decided to remove $k = 6$ and $k = 7$ wavenumbers and power values from all of the spectra generated from every map in our fitting algorithm to be certain the effects from the seams were removed completely.

When testing our composite model, we sometimes noticed a discontinuity or jump between the two linear segments where they did not meet end-to-end for a k_T where χ^2 was minimized. Ideally, the best model fit should produce two segments where the higher wavenumber end of m_1 always meets at the starting low wavenumber of m_2 (see Appendix Figure A.1 Class "X"). We used the algorithm to calculate the intersection of the two best fit line segments, designated as the intersection transition k_X. Classifications "X", "Y", and "Z" correspond to whether $k_X = k_T$, $k_X < k_T$ or $k_X > k_T$, respectively shown in Figure A.1. Calculating the intersection provided initial estimates in the uncertainty of the transition scale, which we compared to the bootstrapping uncertainties.

We explored the wavenumber range of $k = 1 - 1000$ and set $k_{mod} = 3 - 50$ which yields a range for $k_T = 4 - 996$ to report the lowest wavenumber converged

solution. If no converged solution is found, we report "DNC" for does not converge. The uncertainties we reported for m_1, m_2, k_T and k_X were calculated by performing bootstrapping techniques without replacement on all of the best power spectra model fits.

4. Results

We developed qualitative descriptions that grouped the different power spectra fit properties. The four group types were mainly determined by spectra fit parameters m_1 and k_T and allowed us to complete a standardized investigation of power spectra that explored temporal evolution of different spatial distributions. These types are completely separate from the spectra model fit classifications shown in Figure A.1 that focused on a spectrum's fit kinks, k_T and k_X. The four types presented in Table 3 are described here. Type A is characterized by a shallow or flat m_1 value with $m_1 < -0.7$ and a transition scale that is $k_T < 50$. Type B is the opposite of Type A where $m_1 > -0.7$ and the transition scale is $k_T > 50$. Type C is a blend of Type A and Type B where $m_1 < -0.7$ (property of Type A) but the transition scale is found in tight range of $k_T = 50 - 60$ (semi-like property of Type B). Type D does not fit any of the previous types. The spectra fit types and the classifications describe a complete picture of the modeled spectrum fit found by our algorithm. There are a few spectra fits missing from figures that correspond to "DNC" entries. These fits varied over the range of k_{mod} constantly and we did not feel confident in reporting one specific spectra fit's parameters.

One may notice that the Kolmogorov $k^{-5/3}$ relation is missing from type criteria that we just described, which is slightly foreshadowing a finding of our study. While we did not find any instances of m_1=-1.67, we did find that m_2 often matched the Kolmogorov $k^{-5/3}$ relation and we identified these instances with a superscript "E". It is important to note that these convergence types and classifications are subject to the reported uncertainties. The total suite of descriptions were meant to qualitatively group the behavior of the algorithm's results to multiple power spectra.

4.1. Fitting 60°N-60°S

We first limited the latitude range of power spectra that we analyzed to 60°N-60°S. This near global range was chosen to compare power spectra map results to prior studies, Harrington et al. [18] and Choi & Showman [7], and to avoid introducing artifacts from seams present at higher latitudes. We also conducted systemic tests on this set of data to the initial wavenumber k_{low} sensitivity. The right panel of Figure 1 shows there is a high amount of spectral power at $k = 1$ across many latitudes, and sometimes spanning across shear regions. This effect is attributed to large scale sporadic events such as belt revivals and convective disturbances where cloud patterns dominate half the globe [13]. We found that changing $k_{low} = 1$ to $k_{low} = 2$ had a significant impact on the calculated transition wavenumbers; see panels (c) and (d) in Figure 4. In

these cases, most of the spectra kinks were in the range of $k_T = 20 - 100$ with $k_{low} = 2$, while $k_{low} = 1$ found significantly higher valued transitions. Modifying the fits to $k_{low} = 3$, our algorithm found the same transition wavenumbers that were found as when $k_{low} = 2$, and so we chose $k_{low} = 2$ for the rest of our study. This low wavenumber behavior and sensitivity was not fully explored in Barrado-Izagirre et al. [2] and Choi & Showman [7] because they had chosen to set $k_{low} = 10$.

Table 4 shows the energy power spectra fits with $k_{low} = 2$. We have included the energy power spectra fits with $k_{low} = 1$ in tabular form in the Appendix Table A.1. Figure 4 panels (a) and (b) show the fitted slopes as a function of time from these tables with a horizontal dashed line at the Kolmogorov theoretical $k^{-5/3}$ relation. We found low wavenumber slopes in the range of m_1=[-0.3,-0.8] were consistently above theory for all observations. On the other hand, almost all of the slopes at high wavenumbers fall within the range of m_2=[-1.4,-1.7], clustering closer to the theoretical Kolmogorov prediction. The differences in the transition wavenumbers is apparent in panels (c) and (d) of Figure 4 for $k_{low} = 1$ and $k_{low} = 2$, while the slopes remain largely insensitive to this change.

4.2. Latitudinal Limits

We varied the northern and southern boundaries and generated energy power spectra with smaller latitude ranges that symmetrically decreased by 20° such that the energy power spectra spanned latitudes of ±50°, ±40°, ±30°, and ±20°. Incremental changes in latitude ranges of the energy power spectra produced virtually no changes to the derived fit parameters. Figure 5 shows there is no real difference in fit parameters between ±60° and ±20°, which also reaffirms that resolution over a large latitude range does not impact the spectra fits found by the algorithm.

We decided to further tighten the latitude range to just the equatorial zone of Jupiter spanning ±7°, also shown in Figure 5. The equatorial zone had the highest native resolution so we performed additional sensitivity tests to the high wavenumber limit of the fitting algorithm parameter k_{high} (see Appendix). Analyzing just the equatorial zone was also our first exploration at fitting individual zonal wind shear regions on the planet. (Note that throughout the paper, we will refer to shear regions to specifically mean zonal wind shear in Jupiter's zonal wind profile.) Figure 5 shows that combined shear regions have somewhat different values when compared to the equatorial zone, which is purely an anti-cyclonic shear region. Specifically, we see that m_1 is noticeably higher and even becomes positive for the equatorial zone as seen in panel (a) of Figure 5. We also see the equatorial zone have m_2 values that are noticeably lower, and transition wavenumbers of $k_T < 30$ and $k_X < 30$ containing much less scatter than the ±60° and ±20° power spectra fits.

4.3. Zonal Wind Shear Regions - Jupiter's Zones and Belts

Maps made at optical, infrared and radio wavelengths [18, 46, 12, 9] all show Jupiter's well-known banded morphology, seen as intensity fluctuations

as a function of latitude, as shown in Figure 1. Jupiter's "zones" are lighter, generally white, cloudy regions that reside between peaks of Jupiter's zonal winds in anti-cyclonic shear regions. The "belts" on the other hand, are darker and are present over latitude ranges where the zonal winds are in cyclonic shear regions.

We applied a moving average smoothing of 1.1° to all of the zonal wind profiles derived from HST observations between 1994-2015 and then located the relative maxima and minima in the averaged zonal wind profile. The zonal wind profiles from 2015-2017 were separately smoothed and the peaks of the jets also located to serve as a comparison to the the earlier observations. We found that the meridional position of the jets were quite stable and decided to bin their location in increments of 1.0° latitudes. The mapping resolution was set to 0.1° and the latitudes assigned to different shear regions sometimes span several degrees, so any natural variation in jet location of 0.5° would have been detected. Given the latitudinal span of several shear regions, any deviation by a 0.5° shift or smaller would result in only a few latitude FFT scans contributing power from an adjacent shear region and be a rather small effect. The latitude ranges chosen for each shear region are shown in Table 5.

Following the earlier work of Barrado-Izagirre et al. [2] that averaged the spectra of different vorticity regions together, Figure 6 shows energy power spectra best fits for anti-cyclonic and cyclonic regions that were combined over the latitude range of ±56°. There are quantifiable differences in the two different shear region power spectra model fits that indicate distinct dynamical behavior. Figure 6 shows that the anti-cyclonic and cyclonic shear regions typically have similar values of $m_1 \leq -0.8$, where the belts are maybe only slightly steeper. The transition values found for the zones are typically $k_T < 50$ where as the belts have values in the range of $k_T \sim 50 - 100$. Tables 6 and 7 present the specific values for Figure 6. The anti-cyclonic shear region power spectra fits are dominated by type A property fits, while the cyclonic shear regions have a majority of type B and D property fits. A more subtle trend is seen in m_2 values for anti-cyclonic shear regions are generally less than for cyclonic shear regions, especially significant when considering the low uncertainties in m_2.

We further explored the energy power spectra of individual shear regions for just the most recent HST observations, between 2015-2017. We chose these observations because they all had maps from the same 631 nm filter; limiting variations that we did not test for in filter wavelength. Figure 7 shows the results of energy power spectra for January 2015 (rotation a), December 2016 (rotation a), and the averages for all of the derived energy power spectra fits over this time frame. The equatorial zone spectra fits were excluded since they are already shown in Figure 5 and have outlier-like m_1 values that would draw attention away from the smaller, more significant pattern in the fits. The non-shaded and shaded regions in Figure 7 show the zones (anti-cyclonic shear) and belts (cyclonic shear), respectively. The red squares, blue squares, and the black line average mostly alternate as a function of latitude, especially in the northern hemisphere, following the oscillatory nature of the zonal wind profile. Figure 6 showed there is a distinction between the combined zones and belts

on a global scale, but Figure 7 shows there are deviations in latitude where the variations from the global average are statistically significant. Overall, the transition wavenumbers for individual shear regions seem to be slightly higher than the average value. There are a few specific latitude regions where the transition wavenumber is much greater.

5. Discussion

This study found a flat or shallow spectral slope at low planetary wavenumbers in the passive tracer power spectra of Jupiter's clouds, which was unexpected considering traditional turbulence theory. Figure 2 panel (a) does not predict a spectral slope over this wavenumber regime that could offer a sufficient explanation for the presence of low m_1 values we found. Young & Read [47] found that Jupiter's kinetic energy eddy power spectrum appeared to also have a flat spectrum from wavenumbers $k \sim 1 - 30$. The high wavenumber limit of that range was compared to the value of n_{jet} in their work which corresponds to the number of zonal jets in Jupiter's zonal wind profile. A flat spectrum is predicted at low wavenumbers in zonostrophic turbulence generated by a large scale drag or friction on fluids rotating on a sphere [41], but a complete analysis of kinetic energy power spectra would be needed to determine if the low transition wavenumbers found in Figure 2 panel (b) were similar to the frictional meridional wavenumber n_{fr}.

Studies at longer wavelengths by Harrington et al. [18] and Cosentino et al. [9] found transitions in power spectra of $k_T = 26$ in the infrared 5 μm and $k_T = 28$ in the radio 2 cm, respectively. There are several power spectra fits in Table 4 that have low wavenumber transitions near $k_T \sim 30$; considering uncertainty estimates. The Rhines scale noted in Figure 2 panel (a) is the closest theoretical wavenumber to suggest a physical mechanism for the spectral kink in the zonal passive tracer spectra near $k_T \sim 30$ and according to theory is a physical size where the inverse energy cascade might stop or the width of a zonal jet [33, 40].

The transition of power spectra near $k_T \sim 30$ is evident at long wavelength observations probing beneath the cloud deck. While we have successive maps at optical wavelengths in which we can calculate 2-D wind fields, obtaining such maps at long wavelengths is very difficult and the resolution worsens approximately by λ/D, where λ is the wavelength and D is the diameter of the telescope or longest baseline in an array. Calculating 2-D wind fields is also computationally expensive, so our results suggest that one can probe the dynamical state of different layers of Jupiter's atmosphere with single observation maps. Any changes in the passive tracer power spectra ought to be connected to changes in the optical cloud deck and associated winds.

Because the low wavenumber sensitivity of Jupiter's power spectra was not explicitly explored before, it is worthwhile for a future study to take into account the findings of this work and previous studies all finding a low wavenumber transition scale near $k_T \sim 30$. Prior studies underestimated the low planetary wavenumber limit at $k_{low} = 10$. It is clear that starting $k_{low} = 10$ does not find

what appears to be a common power spectrum feature in Jupiter where several studies locate a spectral slope transition near $k_T \sim 30$. Perhaps starting power law fits with $k_{low} = 20 - 30$ and possibly higher, and sequentially increasing k_{low}, would converge to a power spectrum fit at wavenumber ranges not possible to confidently investigate otherwise. It is then possible that the power spectra of Jupiter's atmosphere might be similar to what we propose in panel (b) of Figure 2. That panel presents a theoretical power spectrum of Jupiter, that has multiple spectral kinks with a unique low wavenumber spectral index, which is based on our and others' results. Because we are analyzing a large latitude domain of a gas giant atmosphere and not directly following the transfer of energy, it is not conclusive that at some higher zonal wavenumber that energy is being injected, like the Rossby radius or meso-scale storm complexes [17]. It is also entirely possible that a study which starts with a higher k_{low} might not find a statistically significant transition at all and therefore a $k^{-5/3}$ relation may actually be produced from the downward cascade of enstrophy and continue to higher wavenumbers. We feel, this is a logical next step study to be conducted and test if a transition near $k \sim 400 - 500$ can be detected from $k^{-5/3}$ to k^{-3}, or if the Kolmogorov relation extends to even higher wavenumbers.

This was the first study to separately quantify the power spectra of different shear regions in Jupiter's zonal wind profile, where the anti-cyclonic zones have a statistically significant different behavior than the cyclonic belts. We found all but one of the averaged anti-cyclonic shear region fits in Table 6 had power spectra model fits with type "A", while the cyclonic regions on the other hand in Table 7 have a majority of power spectra fits that are classified by types "B" or "D". The difference in the averaged shear region spectra fits is mostly due to the location of the transition wavenumber k_T where the belts have higher wavenumber transitions than the zones, as seen in Figure 6. These two different dynamical regimes were combined when considering the power spectra fits in Figure 4 and Table 4 and have more occurrences of the $k^{-5/3}$ for m_2 than when separated.

While much can be said about combining different dynamical shear regions together to extract a power spectrum of an atmosphere, we also narrowed the latitude domains to apply our analysis more locally, to individual zones and belts. Figure 7 is mostly consistent with Figure 6; $m_1 < -0.7$ in many zones and belts, and generally transition wavenumbers of $k_T \leq 50$ are found or the low wavenumber transition shown in Figure 2 panel (b). But there are a few differences that are noticeably unique, and most notably is the oscillatory trend evident between zones and belts in all the panels. The individual observations show this trend to be significant for specific observations given their uncertainties, but the average also captures this trend. The different shear regions have fits that mirror the changes in the zonal wind profile as a function of latitude. This may be one of the few ways to quantify the difference in the two different shear regions and also investigate areas of the planet that are temporally more dynamic and change in appearance more often. Two areas that are noticeably standout correspond to the belts north of the 24°N jet and south of the Great Red Spot, which both have high wavenumber transitions where $k_T \sim 100 - 400$.

These higher transitions could indicate a real "forcing scale" where energy is injected into the atmosphere to drive changes in 24°N jet speed, or it could indicate a small scale at which enstrophy is being dissipated by the Great Red Spot as it is shrinking [43, 35]. The Juno mission has found observations showing lightning at higher latitudes, which could be connected to moist convection as a source for injecting energy at these locations [17, 4, 25]. This is another result of our analysis that finds unique power spectra features corresponding to dynamic areas on the planet.

Jupiter's proximity to Earth and the sun allows for us to study turbulence of fine scaled features. We have presented that there are ranges where the Kolmogorov $k^{-5/3}$ relation is found, which is also true for Earth's atmosphere. We also found that at the largest scales Jupiter's passive tracer power spectra are more shallow than classical theory, perhaps being influenced by a large-scale drag or friction according to zonostrophic theory [42, 41]. By contrast, Earth's power spectra for zonal and meridional wind measurements at the largest scales is actually found to be steeper [32]. Larger telescopes and an ice giant mission would provide the data necessary to conduct a similar study like this, and those by Sukoriansky et al. [42], Galperin et al. [15], to investigate if there are similar passive tracer and kinetic energy power spectra for Saturn, Uranus and Neptune.

6. Conclusions

We made full global maps of Jupiter from HST observations in Table 1. The filters chosen analyzed the ammonia ice cloud near 700 hPa. After developing a passive tracer power spectra fitting algorithm we conclude the following:

1. Near global maps ($\sim \pm 60°$), averaged shear regions (belts and zones), and individual shear regions (e.g. NEB) mostly show the presence of a near-flat or shallow power spectral index at low planetary wavenumbers; approximately $k \sim< 20 - 50$.
2. A transition in passive tracer power spectra is typically found $k_T \sim 20-50$. This size is similar to the theoretical Rhines scale. It is not a forcing scale, but a size where the inverse cascade of energy may be halted [33, 40]. A similar transition wavenumber was found in analyses by Harrington et al. [18], Cosentino et al. [9], and Young & Read [47].
3. Jupiter's averaged anti-cyclonic and cyclonic shear regions have distinctly different power spectra parameters; statistically significant differences in m_2 and transition wavenumbers, but share the commonly found $m_1 < -0.7$ property.
4. Spectral analyses of individual shear regions as a function of latitude sometimes find similar transitions near $k_T \sim 20-50$ but also finds some regions with transitions at higher wavenumbers $k_T \sim 100 - 400$. The spectra fit parameters for the high wavenumber slope m_2 and the spectra transitions tend to oscillate in value reflecting changes in the vorticity of the zonal wind profile.

Future studies using a lower wavenumber limit, k_{low}, should start where this shallow or flat spectrum has been observed to end, near $k \sim 20 - 50$. Maybe then, the Kolmogorov theory of turbulence will be apparent in power spectra of Jupiter's atmosphere. A future study should compare these results with kinetic energy power spectra for dates where sufficiently high resolution 2-D maps of the winds can be generated, and be used to complete zonostrophic turbulence analysis. Such a study, will help determine the true nature of turbulence in Jupiter's atmosphere by comparing passive tracer, zonal mean zonal kinetic energy power, and kinetic energy power spectra all to each other. A complete observational and theoretical analysis like that could help determine science objectives of future missions to any of the gas giant planets.

Acknowledgements

Richard Cosentino's research was supported by an appointment to the NASA Postdoctoral Program at the NASA Goddard Space Flight Center, administered by Universities Space Research Association under contract with NASA. Based on observations made with the NASA/ESA Hubble Space Telescope, obtained [from the Data Archive] at the Space Telescope Science Institute, which is operated by the Association of Universities for Research in Astronomy, Inc., under NASA contract NAS 5-26555. These observations are associated with programs in GO5313, 6009, 6452, 11096, 13067, 13937, 14334, 14661, 14756 (chronologically listed), and AR14858. Support for programs 13937/14334/15262 and 14585 was provided by NASA through a grant from the Space Telescope Science Institute. Access to all of the maps produced under these programs are available at https://archive.stsci.edu/prepds/jtps/ and supporting webpages. Additionally, data from our analysis presented in figures and tables from this manuscript are available as supplemental material.

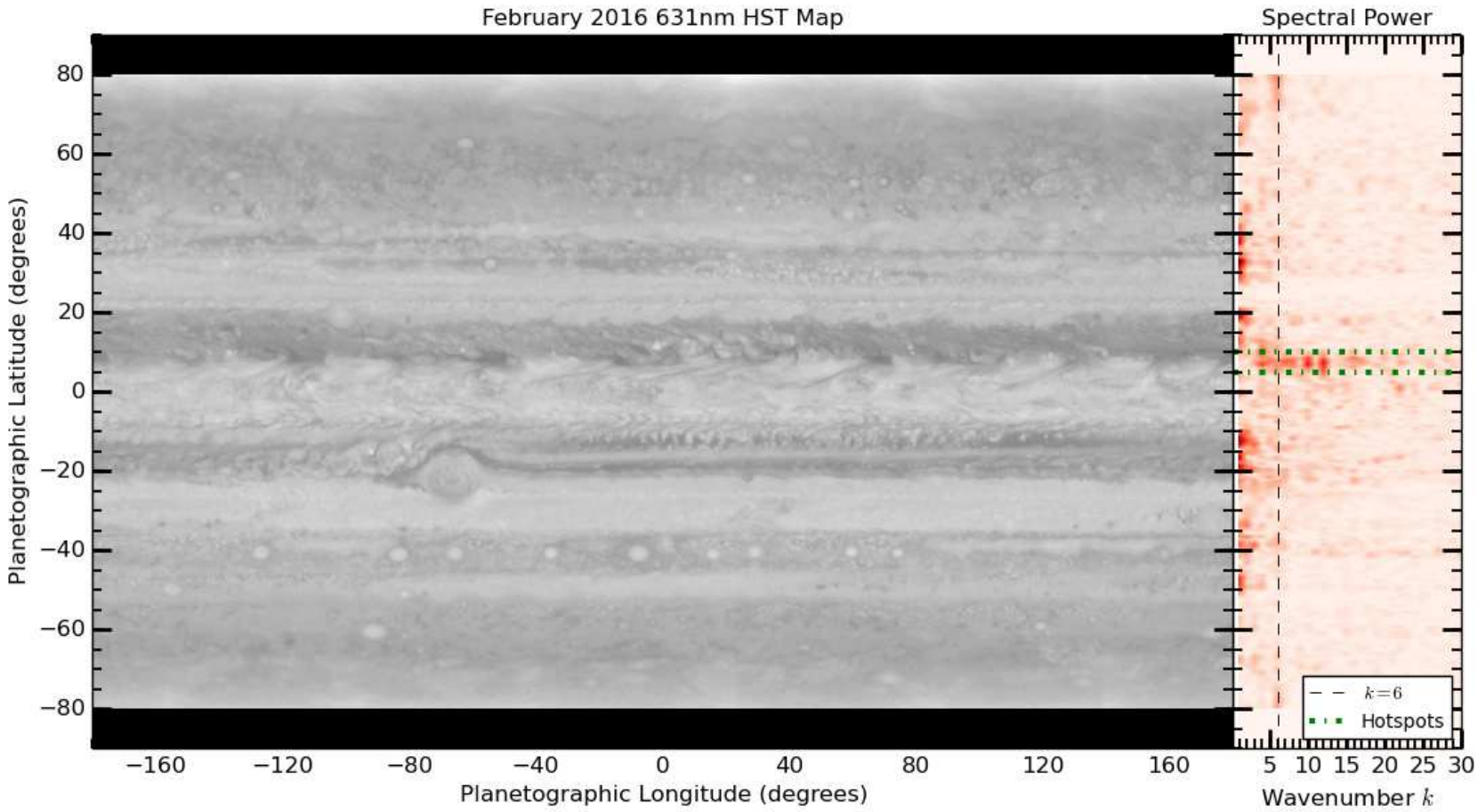

Figure 1: HST OPAL 631nm map from February 2016. Periodic bright areas at high latitudes in the map at the left are artifacts from seam stitching and their associated spectral power in the right panel is present at $k = 6$ (vertical black dashed line). High spectral power at $k = 1$ is seen at several latitudes where half-global patterns produce strong spectral power; near the North Temperature Belt ($\sim 35°$N) and the Great Red Spot. Latitudes 5°-10°N (horizontal green center lines) contain significant spectral power associated with the hotspots.

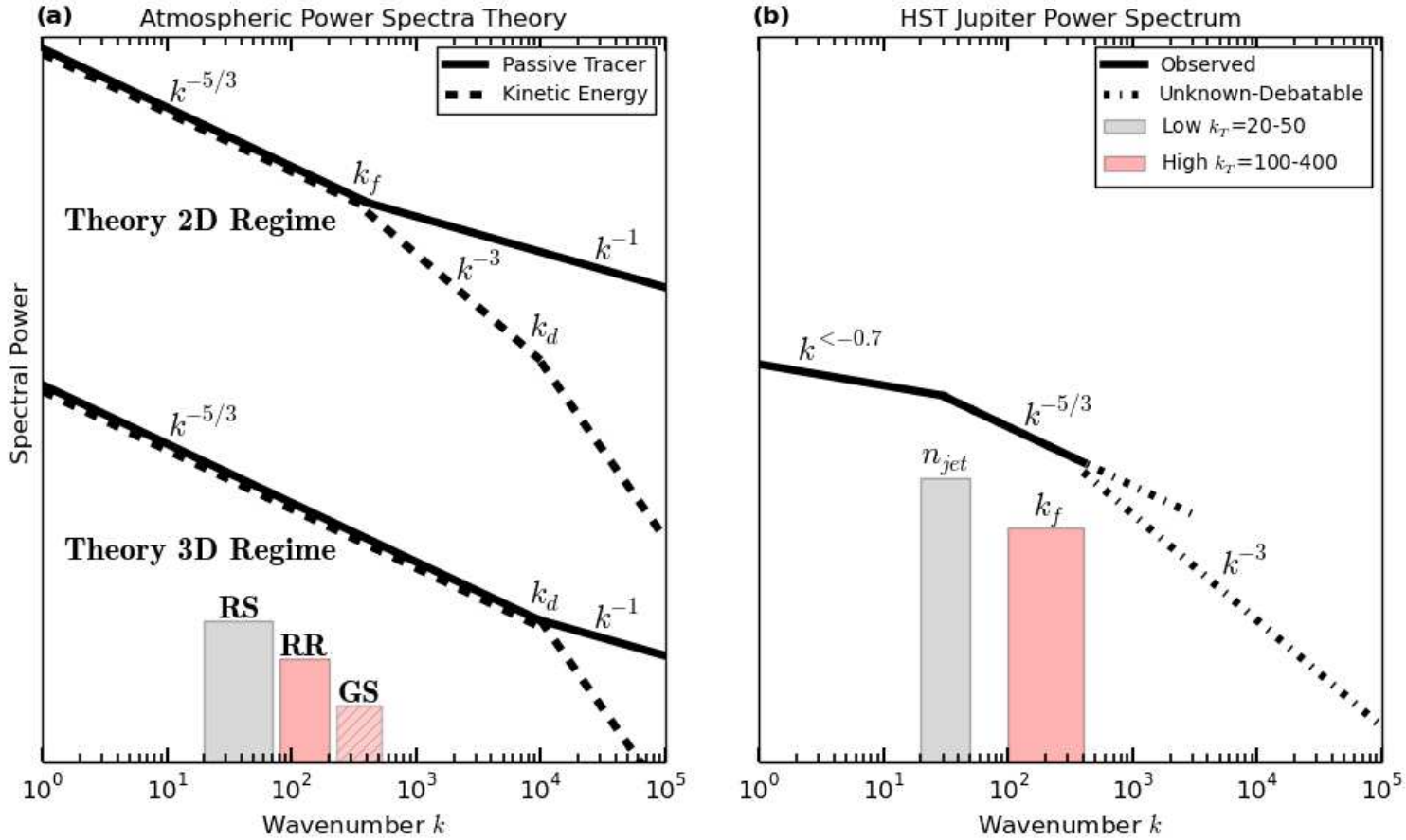

Figure 2: Log-log plots of spectral power versus wavenumber k for passive tracer and kinetic energy power spectra for different dimensional regimes in panel (a). The Rhines scale ("RS" k∼20-70), Rossby radius ("RR" k∼80-180), and a convective storm ("GS" k∼220-450) have their corresponding wavenumber ranges shaded. Panel (b) shows the observed Jovian power spectrum based on results from this paper. A low transition wavenumber $k_T \sim 20 - 50$ (grey shading) was found in many anti-cyclonic shear region spectra and is similar to the number of zonal wind jets $n_{jet} \sim= 28$. Some cyclonic shear region spectra had a higher transition wavenumber $k_T \sim 100 - 400$ which could represent the forcing scale k_f from theory. Regardless of where k_T was found, spectra typically transitioned to slopes near Kolmogorov $k^{-5/3}$ at higher wavenumbers.

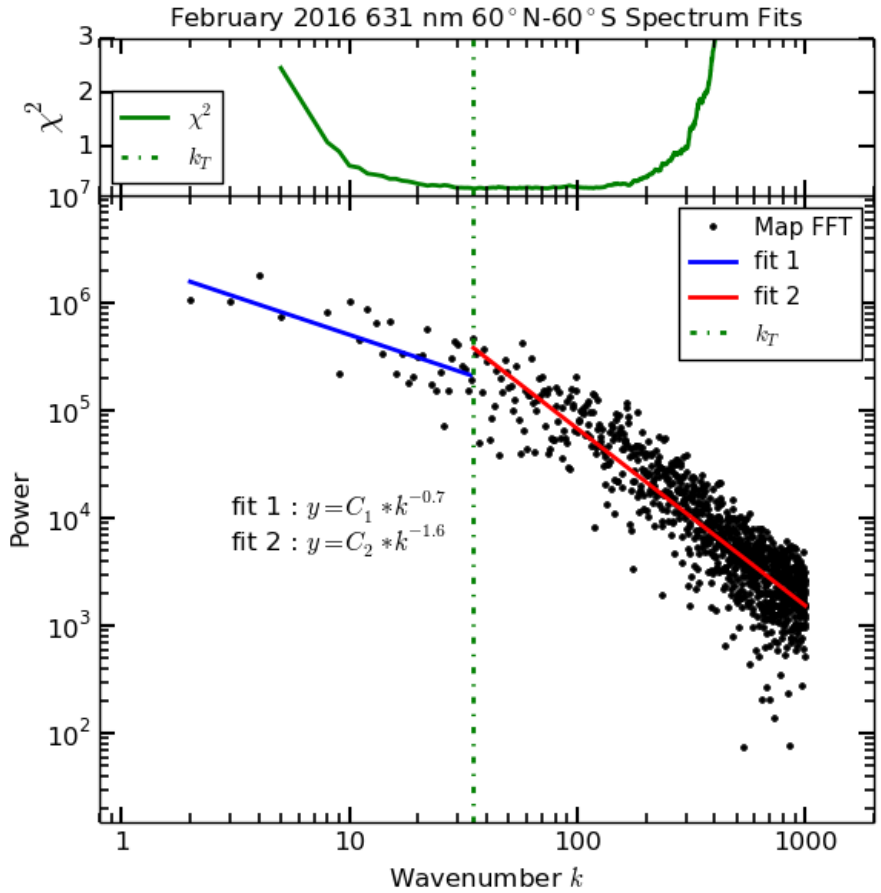

Figure 3: Example passive tracer power spectra for February 2016 observations as black points in the bottom panel, with the best determined fit line segments with slopes m_1 and m_2 in blue and red, respectively. The transition scale is a dot-dashed line that extends upwards and is drawn again in the top panel that shows where χ^2 is minimized.

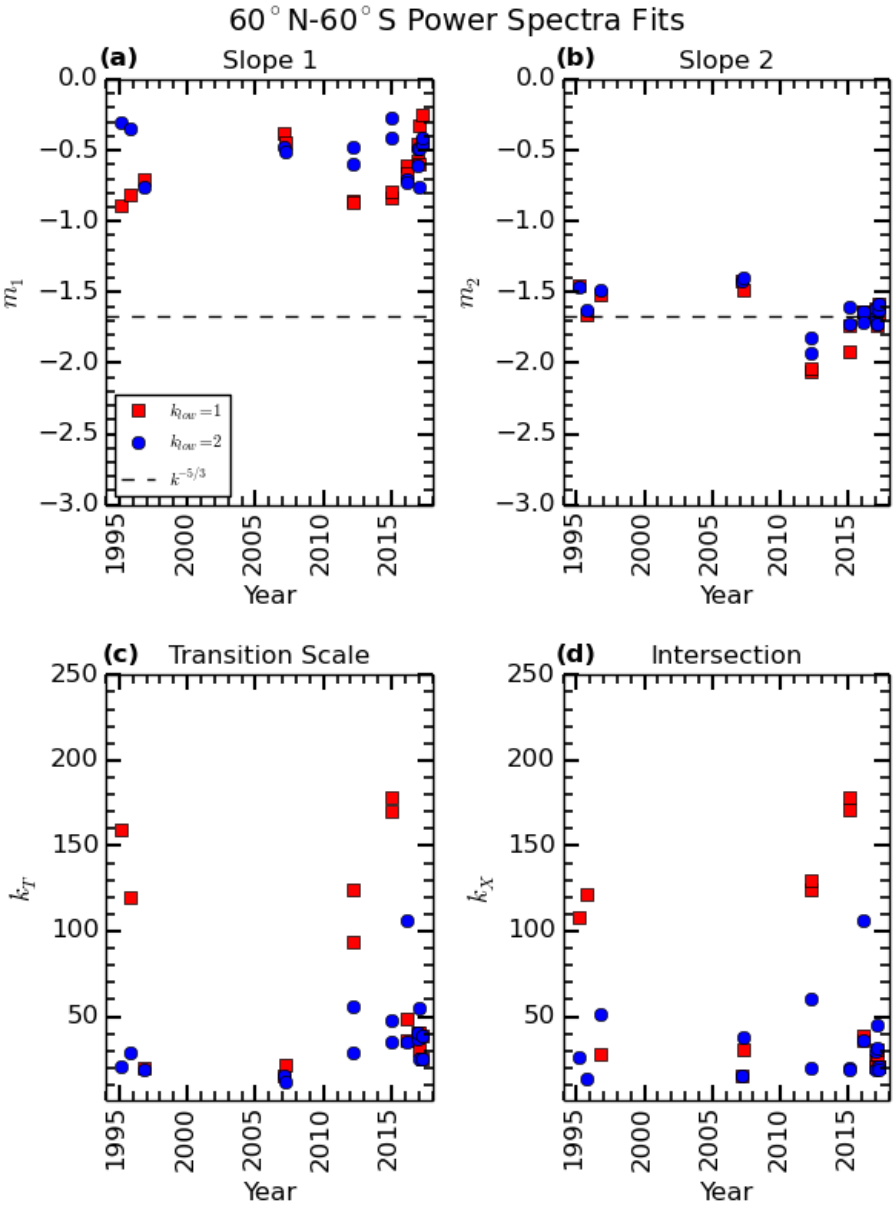

Figure 4: All panels show power spectra fit parameters with $k_{low} = 1$ as red squares and $k_{low} = 2$ as blue circles. Panels (a) and (b) show m_1 and m_2 values, respectively, where the theoretical value of $k^{-5/3}$ from Kolmogorov theory is shown as a dashed horizontal line. Panel (c) shows k_T values and panel (d) shows k_X values. Legend in panel (a) applies to all.

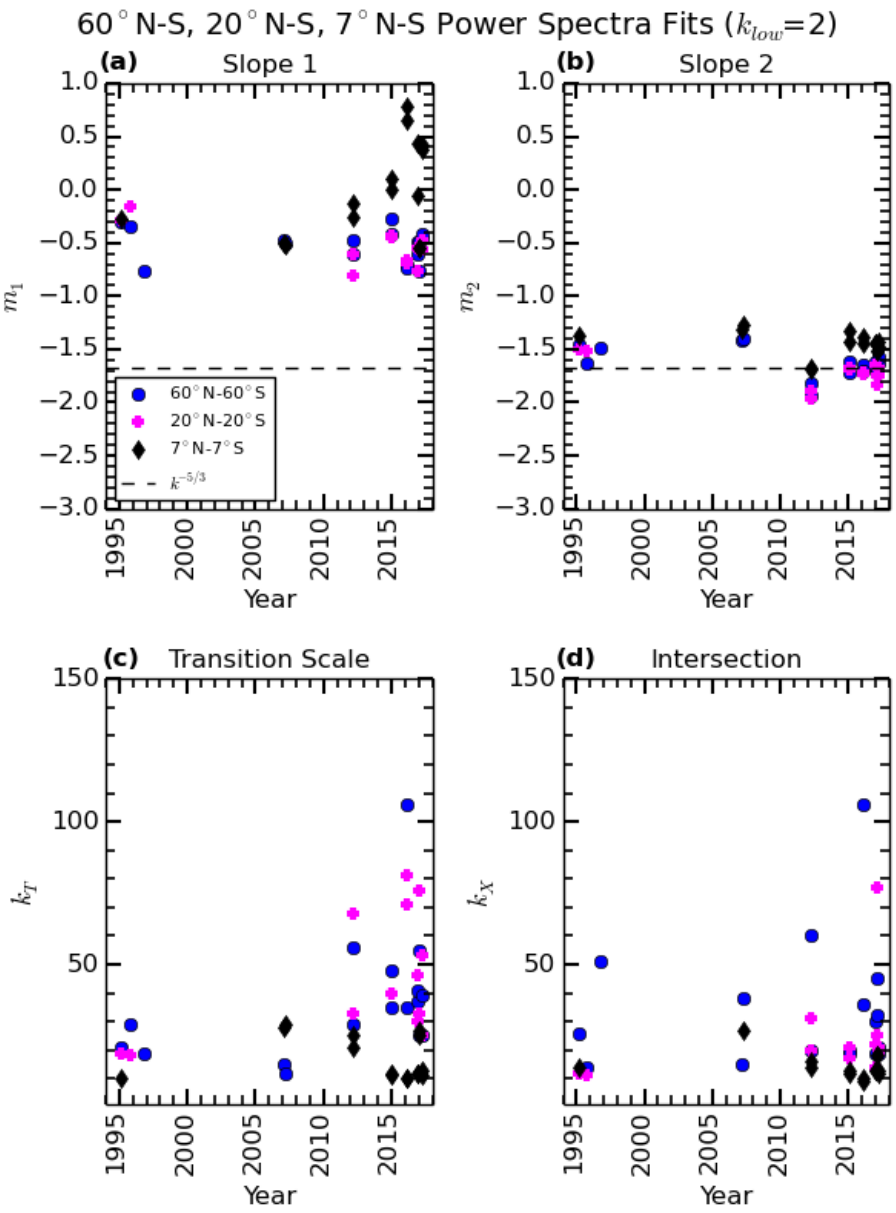

Figure 5: Same as Figure 4 where selected latitudinal regions are shown as different shapes and colors. Power spectra fits shown are for $k_{low} = 2$. Legend in panel (a) applies to all.

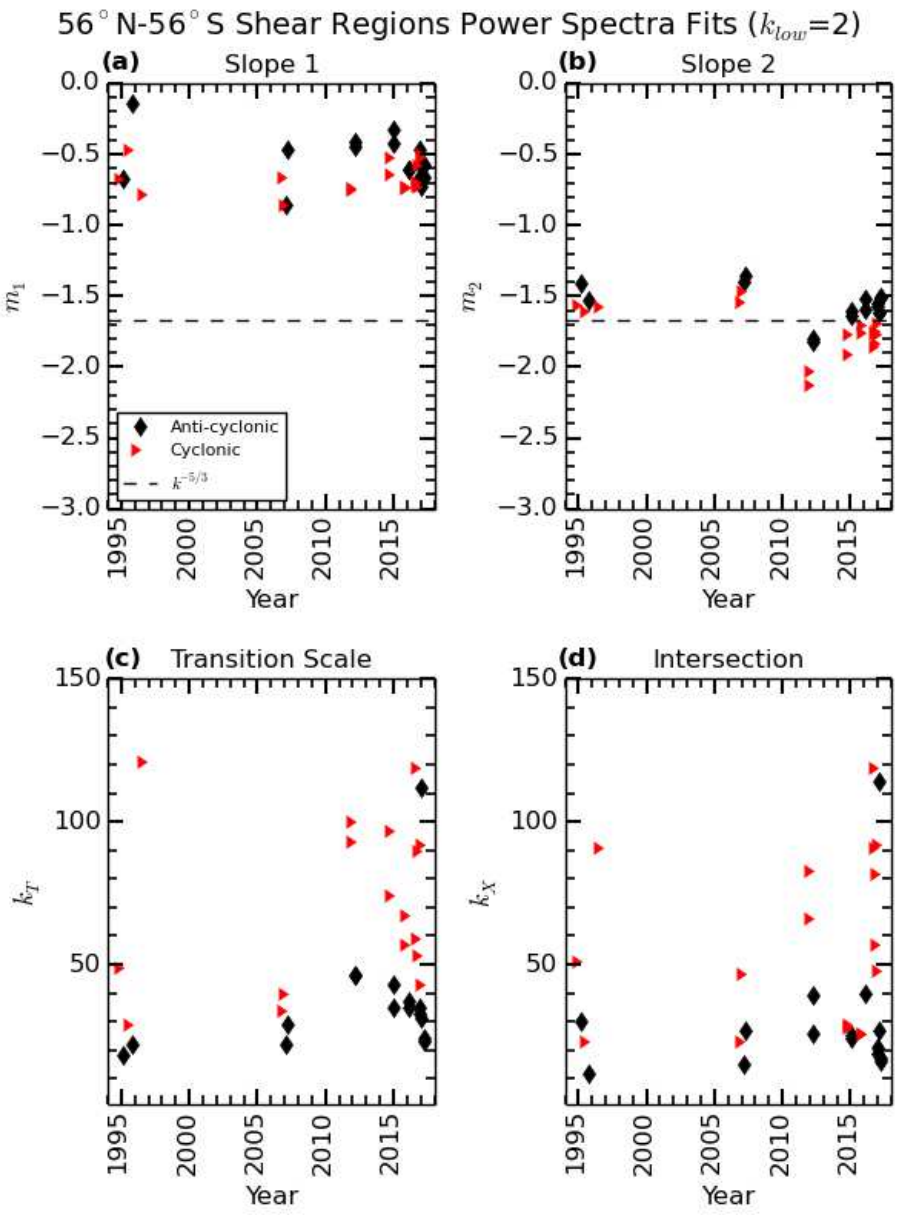

Figure 6: Similar to Figure 5 but for different shear regions; anti-cyclonic (black diamonds) and cyclonic (red triangles). Legend in panel (a) applies to all.

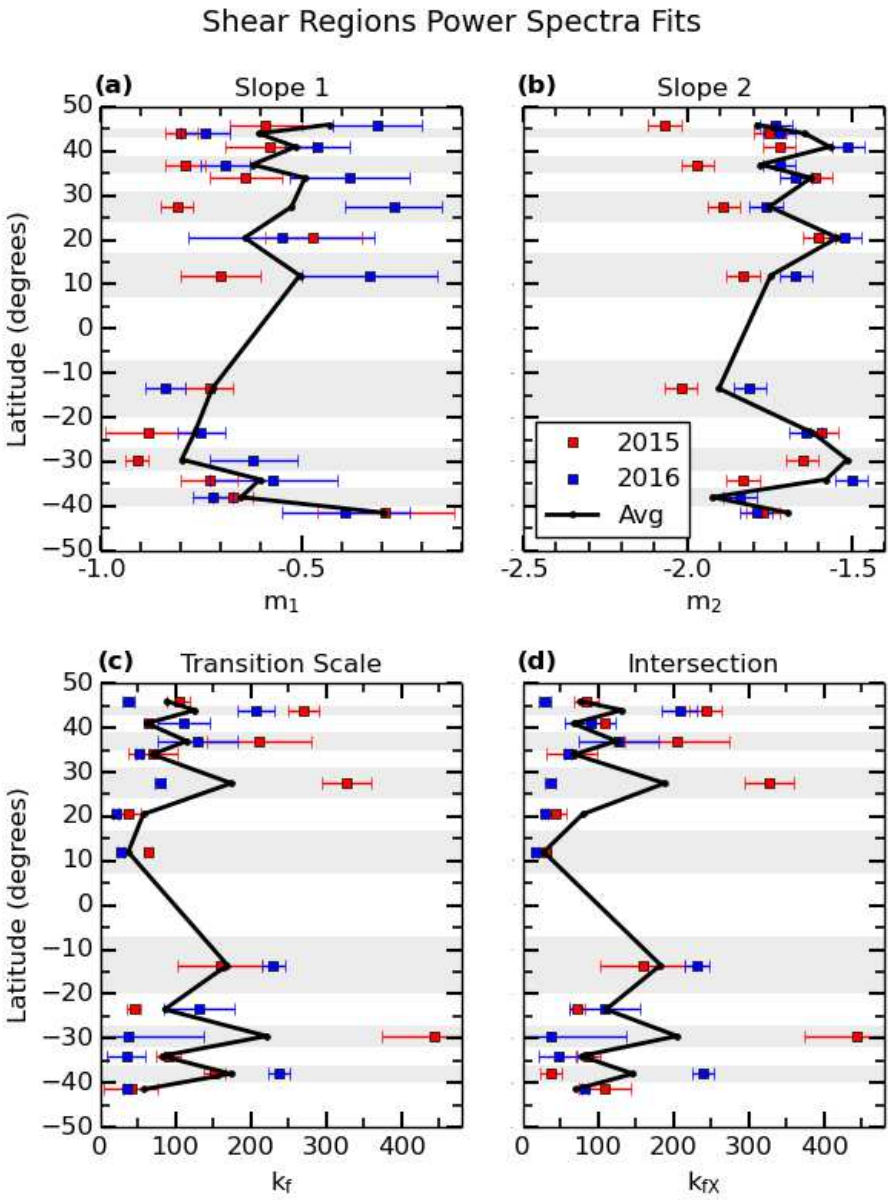

Figure 7: Anti-cyclonic zones (clear) and cyclonic belts (shaded) are shown as a function of latitude where results of each shear region spectra fits from 2015a (red squares) and 2016a (blue squares) are shown with the average of all observations (black line) between 2015-2017.

Table 1
HST Observations

Date (Yr Mo Day)	Date (Decimal)	Filters (nm)	Rotations a or b
1995 Feb 17	1995.13	673, 953	a
1995 Oct 5	1995.76	953	a
1996 Oct 21	1996.8	673, 953	a
2007 Feb 26	2007.15	673, 953	a
2007 Mar 25	2007.23	673, 953	a
2012 Sep 20	2012.72	763	a,b
2015 Jan 19	2015.05	631	a,b
2016 Feb 9	2016.11	631	a,b
2016 Dec 11	2016.96	631	a,b
2017 Feb 1	2017.09	631	a,b
2017 Apr 3	2017.26	631	a,b

Table 1: Observations with 2 rotations will designate consecutive maps as “a” and “b”, while single rotation observation maps will only designated as “a”.

Table 2
Observed Resolution Limit

Date (Decimal)	Range (km)	Focal Length (mm)	Equator Resolution (km / °)	Wavenumber Limit (k_{max})
1995.13[3]	8.25 x 10^8	67999.39	182 / 0.146	1234
1995.76[3]	8.58 x 10^8	67999.39	189 / 0.152	1188
1996.8[3]	8.03 x 10^8	67999.39	177 / 0.142	1268
2007.15[3]	8.13 x 10^8	67999.39	179 / 0.144	1254
2007.23[3]	7.47 x 10^8	67999.39	165 / 0.132	1361
2012.72[2]	7.09 x 10^8	78000	136 / 0.109	1651
2015.05[1]	6.57 x 10^8	78000	126 / 0.101	1782
2016.11[1]	6.81 x 10^8	78000	131 / 0.105	1714
2016.96[3]	8.76 x 10^8	78000	168 / 0.135	1336
2017.09[2]	7.53 x 10^8	78000	145 / 0.116	1548
2017.26[1]	6.67 x 10^8	78000	128 / 0.103	1754

Table 2: All of the observations have a pixel scale of 66.67 mm^{-1}. Three observations with the highest native resolutions, noted by the superscript "1", were additionally analyzed in the Appendix to sensitivity tests that varied the upper wavenumber limit k_{high}. Superscript "2" denotes observations which are marginally oversampled at all latitudes, while the "3" denotes observations that are oversampled. WFPC2 had a resolution of 0.045"/pix and WFC3 had 0.040"/pix.

Table 3
Criteria for Different Power Spectra Types

Type	Slope 1 m_1	Slope 2 m_2	Forcing Scale k_T
A	$<$ -0.7	–	$<$ 50
B	$>$ -0.7	–	$>$ 50
C	$<$ -0.7	–	50-60
D	All others not fit		
E	–	-1.66 $\pm$ 0.04	–

Table 3: Entries with "–" are not characterized by this attribute. Type "D" is described by spectra fits not described by "A-C".

Table 4
60°N-60°S Energy Power Spectra Fits - $k_{low} = 2$

Date (Decimal)	Filters (nm)	Slope 1 m_1	Slope 2 m_2	Spectra Break k_T / k_X	Properties
1995.13a	953	-0.30 ± 0.40	-1.46 ± 0.03	21 / 26	A $k_{mod} = 3 - 17$ X
1995.76a	953	-0.35 ± 0.27	-1.63^{E} ± 0.03	29 / 14	A $k_{mod} = 3 - 25$ Y
1996.8a	953	-0.76 ± 0.27	-1.49 ± 0.03	19 / 51	D $k_{mod} = 3 - 15$ Z
2007.15a	953	-0.48 ± 0.56	-1.42 ± 0.03	15 / 15	A $k_{mod} = 3 - 11$ X
2007.23a	953	-0.51 ± 0.35	-1.40 ± 0.03	12 / 38	A $k_{mod} = 3 - 8$ Z
2012.72a	763	-0.60 ± 0.13	-1.93 ± 0.03	56 / 60	C $k_{mod} = 3 - 48$ X
2012.72b	763	-0.48 ± 0.35	-1.82 ± 0.03	29 / 20	A $k_{mod} = 3 - 24$ Y
2015.05a	631	-0.41 ± 0.11	-1.72^{E} ± 0.03	48 / 20	A $k_{mod} = 3 - 44$ Y
2015.05b	631	-0.27 ± 0.21	-1.61^{E} ± 0.03	35 / 19	A $k_{mod} = 3 - 42$ Y
2016.11a	631	-0.71 ± 0.14	-1.64^{E} ± 0.03	35 / 36	D $k_{mod} = 3 - 31$ X
2016.11b	631	-0.73 ± 0.06	-1.71^{E} ± 0.04	106 / 106	B $k_{mod} = 3 - 50$ X
2016.96a	631	-0.49 ± 0.18	-1.67^{E} ± 0.03	37 / 30	A $k_{mod} = 3 - 34$ X
2016.96b	631	-0.61 ± 0.14	-1.62^{E} ± 0.03	41 / 19	A $k_{mod} = 3 - 37$ Y
2017.09a	631	-0.49 ± 0.10	-1.72 ± 0.03	55 / 45	C $k_{mod} = 3 - 50$ X
2017.09b	631	-0.76 ± 0.13	-1.72 ± 0.03	25 / 32	D $k_{mod} = 3 - 21$ Z
2017.26a	631	-0.46 ± 0.13	-1.65^{E} ± 0.03	39 / 21	A $k_{mod} = 3 - 17$ Y
2017.26b	631	-0.41 ± 0.31	-1.58 ± 0.03	25 / 19	A $k_{mod} = 3 - 17$ X

Table 4: Observations with (a) or (b) designate singular or consecutive rotation maps. The superscript "E" notes spectral slopes near the Kolmogorov relation of $k^{-5/3}$ from theory; uncertainties considered.

Table 5
56°N-56°S Zonal Wind Shear Regions

Latitudes	Zone / Belt	Regional Shear
56-52°N	Zone	Anti-cyclonic
52-47°N	Belt	Cyclonic
47-45°N	Zone	Anti-cyclonic
45-43°N	Belt	Cyclonic
43-39°N	Zone	Anti-cyclonic
39-35°N	Belt	Cyclonic
35-31°N	Zone	Anti-cyclonic
31-24°N	Belt	Cyclonic
24-17°N	Zone	Anti-cyclonic
17-7°N	Belt	Cyclonic
7°N-7°S	Zone	Anti-cyclonic
7-20°S	Belt	Cyclonic
20-27°S	Zone	Anti-cyclonic
27-32°S	Belt	Cyclonic
32-36°S	Zone	Anti-cyclonic
36-40°S	Belt	Cyclonic
40-43°S	Zone	Anti-cyclonic
43-48°S	Belt	Cyclonic
48-52°S	Zone	Anti-cyclonic
52-56°S	Belt	Cyclonic

Table 5: Different shear regions from an average of jet extrema locations.

Table 6
56°N-56°S Anti-cyclonic Shear Regions Power Spectra Fits - $k_{low} = 2$

Date (Decimal)	Filters (nm)	Slope 1 m_1	Slope 2 m_2	Spectra Break k_T / k_X	Properties
1995.13a	953	-0.67 ± 0.15	-1.41 ± 0.03	18 / 30	A $k_{mod} = 3 - 14$ Z
1995.76a	953	-0.14 ± 0.24	-1.53 ± 0.03	22 / 12	A $k_{mod} = 3 - 18$ Y
1996.8a	953	DNC	DNC	DNC	DNC
2007.15a	953	-0.86 ± 0.13	-1.40 ± 0.03	22 / 15	A $k_{mod} = 3 - 18$ Y
2007.23a	953	-0.47 ± 0.12	-1.36 ± 0.03	29 / 27	A $k_{mod} = 6 - 25$ X
2012.72a	763	-0.41 ± 0.10	-1.82 ± 0.03	46 / 26	A $k_{mod} = 3 - 42$ Y
2012.72b	763	-0.44 ± 0.18	-1.80 ± 0.03	46 / 39	A $k_{mod} = 3 - 43$ X
2015.05a	631	-0.42 ± 0.10	-1.64^E ± 0.03	43 / 24	A $k_{mod} = 3 - 39$ Y
2015.05b	631	-0.33 ± 0.37	-1.61^E ± 0.03	35 / 25	A $k_{mod} = 3 - 31$ Y
2016.11a	631	-0.61 ± 0.10	-1.59 ± 0.03	35 / 40	A $k_{mod} = 3 - 31$ X
2016.11b	631	-0.61 ± 0.07	-1.52 ± 0.03	37 / 37	A $k_{mod} = 3 - 31$ X
2016.96a	631	-0.47 ± 0.14	-1.57 ± 0.03	33 / 19	A $k_{mod} = 3 - 29$ Y
2016.96b	631	-0.66 ± 0.08	-1.55 ± 0.03	35 / 21	A $k_{mod} = 3 - 31$ Y
2017.09a	631	-0.73 ± 0.04	-1.62^E ± 0.04	112 / 114	B $k_{mod} = 3 - 50$ X
2017.09b	631	-0.59 ± 0.17	-1.62^E ± 0.03	31 / 27	A $k_{mod} = 3 - 27$ X
2017.26a	631	-0.66 ± 0.35	-1.51 ± 0.03	24 / 17	A $k_{mod} = 3 - 20$ Y
2017.26b	631	-0.57 ± 0.31	-1.51 ± 0.03	23 / 16	A $k_{mod} = 3 - 19$ Y

Table 6: Observations with (a) or (b) designate singular or consecutive rotation maps. The superscript "E" notes spectral slopes near the Kolmogorov relation of $k^{-5/3}$ from theory; uncertainties considered.

Table 7
56°N-56°S Cyclonic Shear Regions Power Spectra Fits - $k_{low} = 2$

Date (Decimal)	Filters (nm)	Slope 1 m_1	Slope 2 m_2	Spectra Break k_T / k_X	Properties
1995.13a	953	-0.67 ± 0.07	-1.56 ± 0.03	49 / 51	A $k_{mod} = 3 - 45$ X
1995.76a	953	-0.47 ± 0.14	-1.60^{E} ± 0.03	29 / 23	A $k_{mod} = 3 - 25$ X
1996.8a	953	-0.78 ± 0.20	-1.57 ± 0.04	121 / 91	B $k_{mod} = 3 - 50$ Y
2007.15a	953	-0.66 ± 0.10	-1.54 ± 0.03	34 / 23	A $k_{mod} = 3 - 30$ X
2007.23a	953	-0.86 ± 0.07	-1.46 ± 0.03	40 / 47	D $k_{mod} = 3 - 36$ X
2012.72a	763	-0.75 ± 0.07	-2.03 ± 0.04	93 / 83	B $k_{mod} = 3 - 50$ X
2012.72b	763	-0.74 ± 0.07	-2.12 ± 0.04	100 / 66	B $k_{mod} = 3 - 50$ Y
2015.05a	631	-0.64 ± 0.10	-1.91 ± 0.04	97 / 29	D $k_{mod} = 3 - 25$ Y
2015.05b	631	-0.52 ± 0.11	-1.77 ± 0.03	74 / 28	D $k_{mod} = 3 - 24$ Y
2016.11a	631	-0.73 ± 0.16	-1.70^{E} ± 0.03	57 / 26	B $k_{mod} = 3 - 22$ Y
2016.11b	631	-0.74 ± 0.08	-1.76 ± 0.03	67 / 26	B $k_{mod} = 3 - 22$ Z
2016.96a	631	-0.69 ± 0.04	-1.76 ± 0.03	59 / 91	C $k_{mod} = 3 - 50$ Z
2016.96b	631	-0.72 ± 0.06	-1.85 ± 0.04	119 / 119	B $k_{mod} = 3 - 50$ X
2017.09a	631	-0.58 ± 0.06	-1.75 ± 0.03	53 / 57	C $k_{mod} = 3 - 50$ X
2017.09b	631	-0.73 ± 0.04	-1.83 ± 0.04	90 / 82	D $k_{mod} = 3 - 50$ X
2017.26a	631	-0.50 ± 0.07	-1.77 ± 0.04	92 / 92	D $k_{mod} = 3 - 50$ X
2017.26b	631	-0.52 ± 0.15	-1.69^{E} ± 0.03	43 / 48	A $k_{mod} = 3 - 39$ X

Table 7: Observations with (a) or (b) designate singular or consecutive rotation maps. The superscript "E" notes spectral slopes near the Kolmogorov relation of $k^{-5/3}$ from theory; uncertainties considered.

Appendix A. Systematics and Sensitivity Tests

We tested many parameters of the algorithm systematically to determine which were more sensitive than others. One of the more complicated parameters was the length fit of a line segment, which can be examined by considering an example spectrum. The example spectrum will have only 100 data points from k=1-100 where the algorithm for our example spectrum found a transition scale at $k_T = 23$. The first limitation imposed by varying a line segment (k_{mod}) is that it actually constricts where k_T is found. If k_{mod}=10, then the possible range of allowable k_T exists between k=10-90, since no break can be found at wavenumbers outside of this range, so our choice of k_T=23 is valid.

If k_{mod} is then increased over a range of k_{mod}=10-30, the same best model fit would be found for all $k_{mod} < 12$ finding the transition at $k_T = 23$. When exploring higher values of $k_{mod} > 12$, the model length would pass this transition scale at $k_T = 23$ and force the best model fit to increase the transition scale to a higher wavenumber. Sometimes k_T in those instances would incrementally increase or abruptly change to a higher transition wavenumber. This convinced us to manually investigate all of the best fits over the range of k_{mod}. We reported the lowest k_T over a range of k_{mod} that converged to be the best model fit for a particular power spectrum. We used an automated process to quantify the systematics of the algorithm's response to various sensitivity tests by recording the mode of all possible model fit parameters over a k_{mod} range, as is shown later for resolution effects. Sometimes the modal best fit was the same we found through manual inspection and sometimes they were different. We utilized manual inspection where we found converged results at lower values of k_{mod} that were scientifically significant and reported mode results over higher values of k_{mod} that explored the systematics of the algorithm. We specifically mentioned which reported values we used and why in the paper.

Figure A.1 details different spectra fits by comparing the values of k_X and k_T. Instances when $k_X = k_T$ were classified as as "X" in Figure A.1. When $k_X < k_T$ or $k_X > k_T$, these were classified as "Y" and "Z" respectively. Not only did k_X provide context for the best fit model to a spectrum but it also served as an initial estimate in the uncertainty of k_T which was comparable to the bootstrapping uncertainty found.

We performed additional sensitivity tests to the analysis presented earlier in the paper where we wanted to know if observational resolution had an impact on our results by analyzing the maps from dates with the superscript "1" in Table 2. Figure A.2 shows the results of varying the upper wavenumber limit k_{high} for the equatorial zone $\pm 7^\circ$ over the range k_{high}=500, 1000, and 1500 for two different values of k_{low}. Because we are investigating the algorithm's sensitivity and systematics we decided to use an automated approach and plot the values from the mode of all of the solutions over the range of $k_{mod} = 3 - 50$, instead of the converged solution which is dependent on low wavenumber spectral power. We narrowed the range of plotted slope values and inserted small horizontal offsets for each k_{high} value in Figure A.2. The red squares for $k_{low} = 1$ and the blue circles for $k_{low} = 2$ overlap for almost every case showing there is no large

effect on the modal solution for different k_{high} values.

Because of the results from the equatorial zone, we performed a similar sensitivity test to the shear regions for the same observations because of the significance of that result. Figure A.3 again shows the modal results of those tests with k_{low}=2 as was presented in Figure A.2. The anti-cyclonic shear regions (black diamonds) and cyclonic shear regions (red triangles) show that most of the cases overlap with each other again, and there are but a few instances of a small deviation in the value of a particular parameter. It is clear that the convergence in the equatorial zone exceeds that of the shear regions after being subjected to these sensitivity tests, possibly due to projection effects at the highest latitudes. The high wavenumber limit sensitivity starts to approach k_{max} at latitudes greater than 60°, but only marginally where the lowest k_{max}=818. A common property in both Figure A.3 and Figure 6 is the clear distinction in m_2 values between the two different shear regions. The behavior in the transition scales also appears to change between Figure A.3 and Figure 6 and that is mainly due to the range of k_{mod} and choosing to select the mode of possible model fits versus the converged solution through manual inspection.

As mentioned earlier, the model fit results of the 60°N-60°S for the global maps with k_{low}=1 are shown in Table A.1. Table A.1 shows that fits with k_{low}=1 generally have higher wavenumber transition scales which was also shown in Figure 4. We can see there are sometimes steeper m_1 and this is caused from high power at k=1 which forces m_1 to become steep and therefore find better fits at higher transition scales.

We explored increasing the contrast of the April 3, 2017 HST rotation (a) 631 nm map. Table A.2 shows three different contrast levels, "Normal" which is the unchanged image, "High" where we increased the contrast, and "Saturated" where we increased the contrast to the point that some pixels became saturated. The histogram properties are in 8-bit scaled brightness in the 0-255 range. We included fits over the entire length of $k_{mod} = 3 - 50$. Table A.2 shows that increasing the contrast did not alter the power spectra fits outside of each value's respective uncertainty estimates.

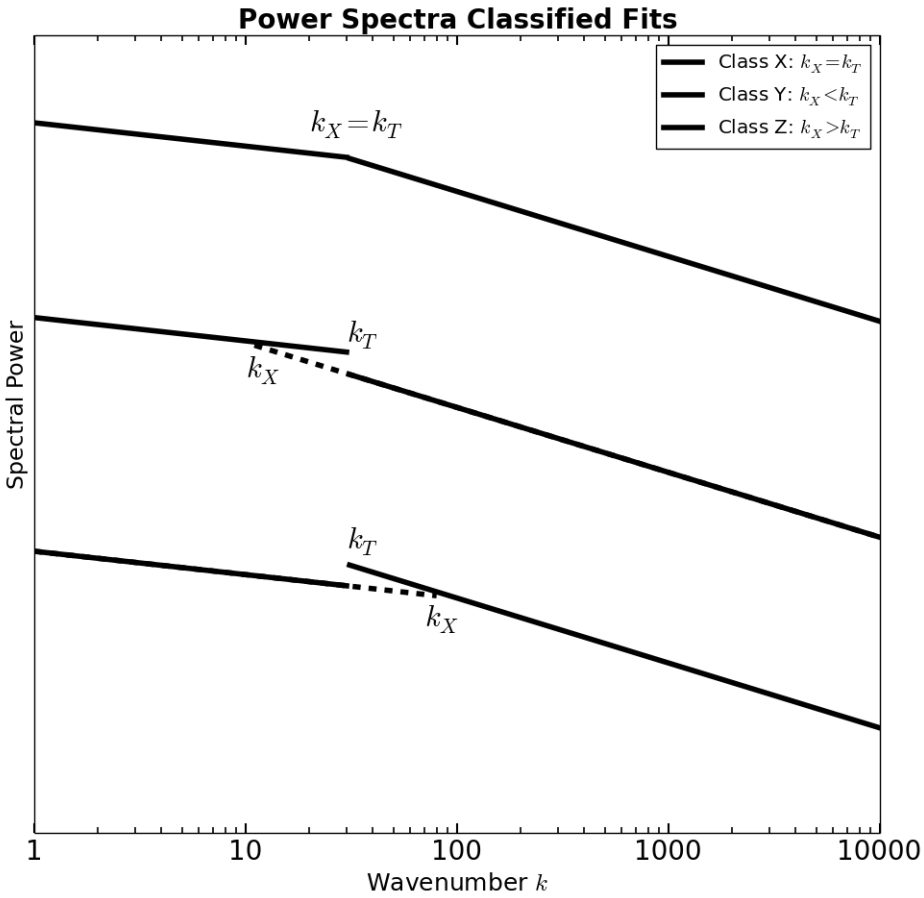

Figure A.1: Log-log plot of spectral power versus wavenumber k for different classifications of spectra fits "X,Y or Z" set by the locations of k_X and k_T relative to each other. Class "X" is the instance of $k_X = k_T$. Two other cases shown lower in plot have dashed lines extending one of the line segments to the intersection and are either classified as "Y" or "Z" fits. The slopes for each segment were unchanged in each classification.

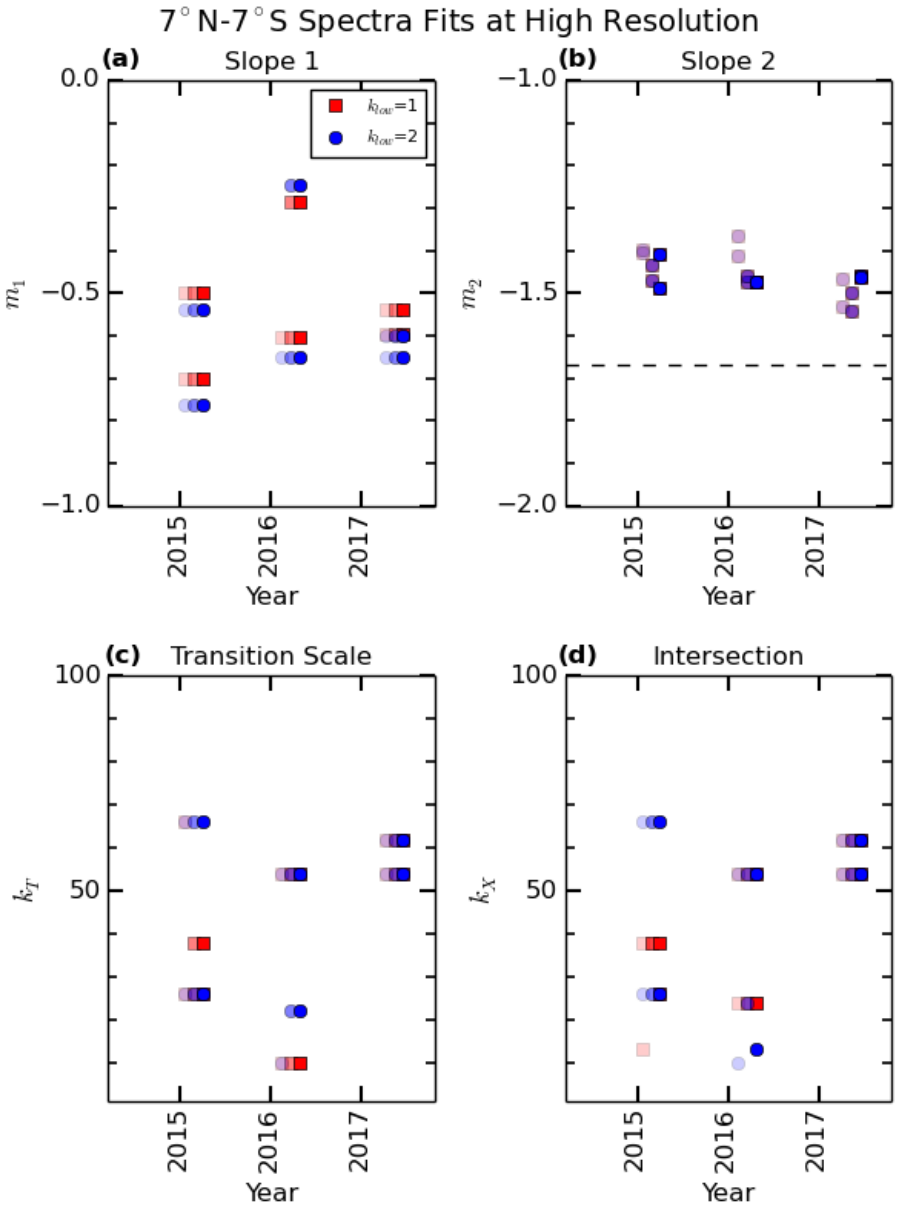

Figure A.2: Results for the equatorial zone with k_{low}=1 (red squares) and k_{low}=2 (blue circles) that show an overall convergence for different high wavenumber limits (k_{high}) in fitting the power spectra. Small horizontal offsets from left to right, also lighter to darker, correspond to values of k_{high}=500, 1000, and 1500.

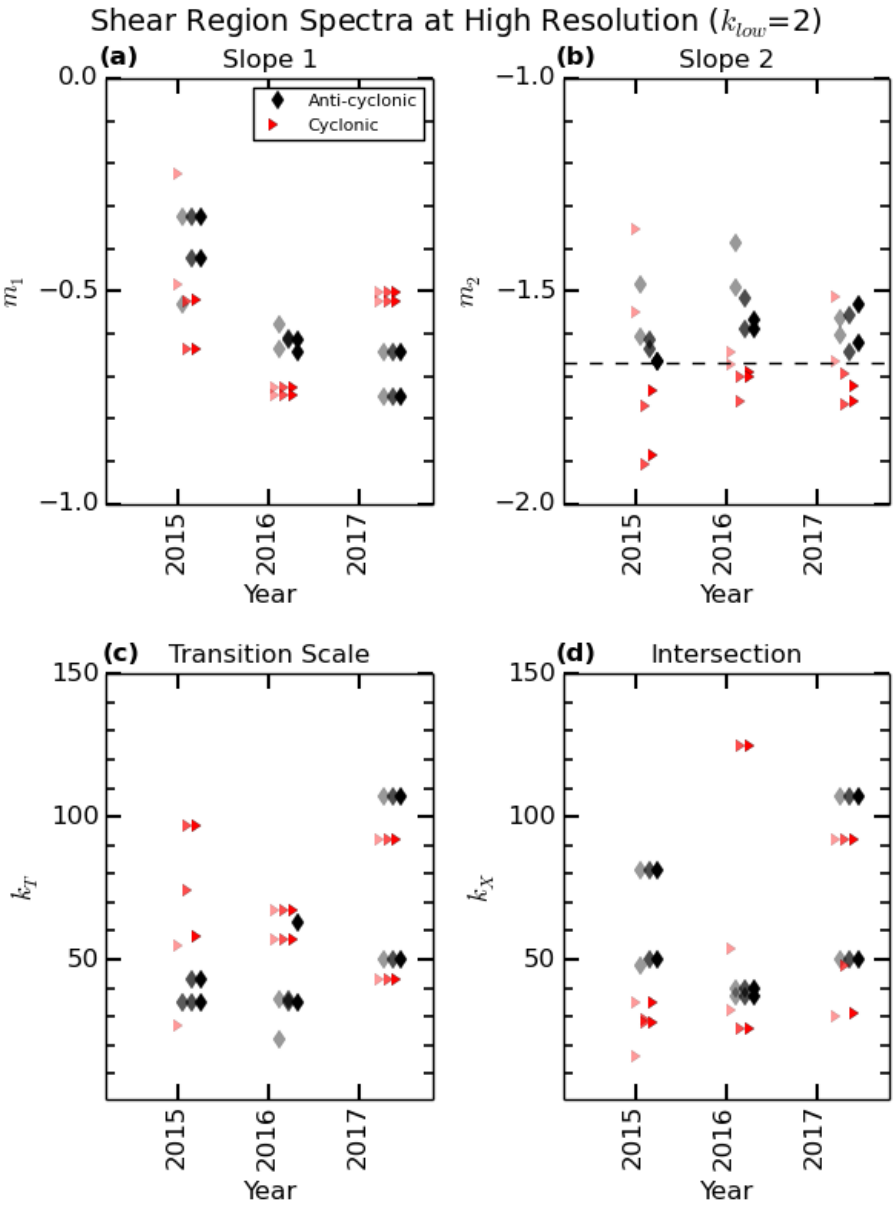

Figure A.3: Results for different anti-cyclonic (black diamonds) and cyclonic (red triangles) shear regions with k_{low}=2 that show an overall convergence for different high wavenumber limits (k_{high}) in fitting the power spectra. Small horizontal offsets from left to right, also lighter to darker, correspond to values of k_{high}=500, 1000, and 1500.

Table A.1
60°N-60°S Energy Power Spectra Fits for $k_{low} = 1$

Date (Decimal)	Filters (nm)	Slope 1 m_1	Slope 2 m_2	Spectra Break k_T / k_X	Properties
1995.13a	953	-0.89 ± 0.06	-1.45 ± 0.04	159 / 108	B $k_{mod} = 3 - 48$ Y
1995.76a	953	-0.81 ± 0.07	-1.66^E ± 0.04	120 / 122	B $k_{mod} = 3 - 48$ X
1996.8a	953	-0.92 ± 0.05	-1.38 ± 0.05	203 / 203	B $k_{mod} = 3 - 48$ X
2007.15a	953	-0.38 ± 0.30	-1.42 ± 0.02	15 / 15	A $k_{mod} = 3 - 12$ X
2007.23a	953	-0.47 ± 0.24	-1.40 ± 0.03	19 / 14	A $k_{mod} = 3 - 16$ Y
2012.72a	763	-0.86 ± 0.06	-2.06 ± 0.04	124 / 124	B $k_{mod} = 3 - 48$ X
2012.72a	763	-0.87 ± 0.10	-2.04 ± 0.04	94 / 130	B $k_{mod} = 3 - 48$ Z
2015.05a	631	-0.84 ± 0.04	-1.92 ± 0.05	178 / 178	B $k_{mod} = 3 - 40$ X
2015.05b	631	-0.79 ± 0.07	-1.74 ± 0.04	170 / 171	B $k_{mod} = 3 - 48$ X
2016.11a	631	-0.61 ± 0.12	-1.64^E ± 0.03	36 / 36	A $k_{mod} = 3 - 33$ X
2016.11b	631	-0.66 ± 0.28	-1.64^E ± 0.03	49 / 39	A $k_{mod} = 3 - 46$ Y
2016.96a	631	-0.45 ± 0.11	-1.67^E ± 0.03	37 / 24	A $k_{mod} = 3 - 34$ Y
2016.96b	631	-0.57 ± 0.09	-1.62 ± 0.03	41 / 21	A $k_{mod} = 3 - 38$ Y
2017.09a	631	-0.32 ± 0.17	-1.69^E ± 0.03	41 / 28	A $k_{mod} = 3 - 38$ Y
2017.09a	631	-0.60 ± 0.11	-1.73 ± 0.03	31 / 31	A $k_{mod} = 3 - 28$ X
2017.26a	631	-0.44 ± 0.08	-1.65^E ± 0.03	39 / 21	A $k_{mod} = 3 - 26$ Y
2017.26b	631	-0.25 ± 0.24	-1.58 ± 0.03	25 / 21	A $k_{mod} = 3 - 22$ Y

Table A.1: Observations with (a) or (b) designate singular or consecutive rotation maps. The superscript "E" notes spectral slopes near the Kolmogorov relation of $k^{-5/3}$ from theory; uncertainties considered.

Table A.2
56°N-56°S Anti-Cyclonic Shear Regions Contrast Enhancement
2017.26a 631 nm Energy Power Spectra Fits for $k_{low} = 2$

Contrast	Mean 8-bit	Median 8-bit	Std Dev 8-bit	Slope 1 m_1	Slope 2 m_2	Spectra Break k_T / k_X	k_{mod}
Normal	146.9	162.0	54.1	-0.66 ± 0.35	-1.51 ± 0.03	24 / 17	3-20
Normal	146.9	162.0	54.1	-0.75 ± 0.08	-1.64 ± 0.04	107 / 107	21-50
High	159.3	175.0	59.8	-0.66 ± 0.33	-1.49 ± 0.03	24 / 17	3-20
High	159.3	175.0	59.8	-0.75 ± 0.08	-1.60 ± 0.04	107 / 107	21-50
Saturated	177.9	194.0	68.2	-0.66 ± 0.35	-1.49 ± 0.03	24 / 17	3-20
Saturated	177.9	194.0	68.2	-0.75 ± 0.08	-1.60 ± 0.04	107 / 107	21-50

Table A.2: The units for image histogram properties are listed as 8-bit scaled brightnesses.

[1] Atkinson, D. H., Pollack, J. B., & Seiff, A. 1998, Journal of Geophysics Research, 103, 22911

[2] Barrado-Izagirre, N., Pérez-Hoyos, S., & Sánchez-Lavega, A. 2009, Icarus, 202, 181

[3] Bolton, S. J., Adriani, A., Adumitroaie, V., et al. 2017, Science, 356, 821

[4] Brown, S., Janssen, M., Adumitroaie, V., et al. 2018, Nature, 558, 87

[5] Busse, F. H. 1976, Icarus, 29, 255

[6] Charney, J. G. 1971, Journal of the Atmospheric Sciences, 28, 1087

[7] Choi, D. S., & Showman, A. P. 2011, Icarus, 216, 597

[8] Choi, D. S., Showman, A. P., Vasavada, A. R., & Simon-Miller, A. A. 2013, Icarus, 223, 832

[9] Cosentino, R. G., Butler, B., Sault, B., et al. 2017, Icarus, 292, 168

[10] de Pater, I., DeBoer, D., Marley, M., Freedman, R., & Young, R. 2005, Icarus, 173, 425

[11] de Pater, I., Dunn, D., Romani, P., & Zahnle, K. 2001, Icarus, 149, 66

[12] de Pater, I., Sault, R. J., Butler, B., DeBoer, D., & Wong, M. H. 2016, Science, 352, 1198

[13] Fletcher, L. N., Orton, G. S., Rogers, J. H., et al. 2017, ArXiv e-prints

[14] Friedson, A. J. 2005, Icarus, 177, 1

[15] Galperin, B., Young, R. M. B., Sukoriansky, S., et al. 2014, Icarus, 229, 295

[16] Gierasch, P. J., & Conrath, B. J. 1993, Journal of Geophysical Research (Planets), 98, 5459

[17] Gierasch, P. J., Ingersoll, A. P., Banfield, D., et al. 2000, Nature, 403, 628

[18] Harrington, J., Dowling, T. E., & Baron, R. L. 1996, Icarus, 124, 32

[19] Ingersoll, A. P., & Cuzzi, J. N. 1969, Journal of Atmospheric Science, 26, 981

[20] Ingersoll, A. P., Gierasch, P. J., Banfield, D., Vasavada, A. R., & Galileo Imaging Team. 2000, Nature, 403, 630

[21] Ingersoll, A. P., Dowling, T. E., Gierasch, P. J., et al. 2004, in Jupiter: The Planet, Satellites, and Magnetosphere, ed. F. Bagenal, W. McKinnon, & T. E. Dowling (Cambridge: Cambridge University Press)

[22] Johnson, P. E., Morales-Juberas, R., Simon, A., et al. 2018, Planetary and Space Science, 155, 2 , surfaces, atmospheres and magnetospheres of the outer planets, their satellites and ring systems: Part XII

[23] Kaspi, Y., Galanti, E., Hubbard, W. B., et al. 2018, Nature, 555, 223

[24] Kim, K. K., & Orlando, W. W. 2003, Discrete and Continuous Dynamical Systems, 3, 145

[25] Kolmašová, I., Imai, M., Santolík, O., et al. 2018, Nature Astronomy

[26] Kolmogorov, A. 1941, Akademiia Nauk SSSR Doklady, 30, 301

[27] Kolmogorov, A. N. 1991, Proceedings: Mathematical and Physical Sciences, 434, 15

[28] Lewis, J. S. 1969, Icarus, 10, 365

[29] Li, C., Ingersoll, A., Janssen, M., et al. 2017, Geophysical Research Letters, 44, 5317

[30] Little, B., Anger, C. D., Ingersoll, A. P., et al. 1999, Icarus, 142, 306

[31] Liu, J., & Schneider, T. 2015, Journal of the Atmospheric Sciences, 72, 389

[32] Nastrom, G. D., Jasperson, W. H., & Gage, K. S. 1986, Journal of Geophysical Research: Atmospheres, 91, 13201

[33] Rhines, P. B. 1975, Journal of Fluid Mechanics, 69, 417

[34] Showman, A. P., & Dowling, T. E. 2000, Science, 289, 1737

[35] Simon, A. A., Tabataba-Vakili, F., Cosentino, R., et al. 2018, Astro. Journal, 155, 151

[36] Simon, A. A., Wong, M. H., & Orton, G. S. 2015, Astrophysical Journal, 812, article id. 55

[37] Simon-Miller, A. A., Conrath, B., Gierasch, P. J., & Beebe, R. F. 2000, Icarus, 145, 454

[38] Simon-Miller, A. A., & Gierasch, P. J. 2010, Icarus, 210, 258

[39] Simon-Miller, A. A., Rogers, J. H., Gierasch, P. J., et al. 2012, Icarus, 218, 817

[40] Sukoriansky, S., Dikovskaya, N., & Galperin, B. 2007, Journal of the Atmospheric Sciences, 64, 3312

[41] Sukoriansky, S., Dikovskaya, N., Grimshaw, R., & Galperin, B. 2012, AIP Conference Proceedings, 1439, 111

[42] Sukoriansky, S., Galperin, B., & Dikovskaya, N. 2002, Physical Review Letters, 89, 124501

[43] Tollefson, J., Wong, M. H., de Pater, I., et al. 2017, Icarus, 296, 163

[44] Vallis, G. K., & Maltrud, M. E. 1993, Journal of Physical Oceanography, 23, 1346

[45] Vallis, G. K. V. 2006, Atmospheric and Oceanic Fluid Dynamics (Cambridge University Press)

[46] Vasavada, A. R., & Showman, A. P. 2005, Reports on Progress in Physics, 68, 1935

[47] Young, R. M. B., & Read, P. L. 2017, Nature Physics, 13, 1135

Figure 1.

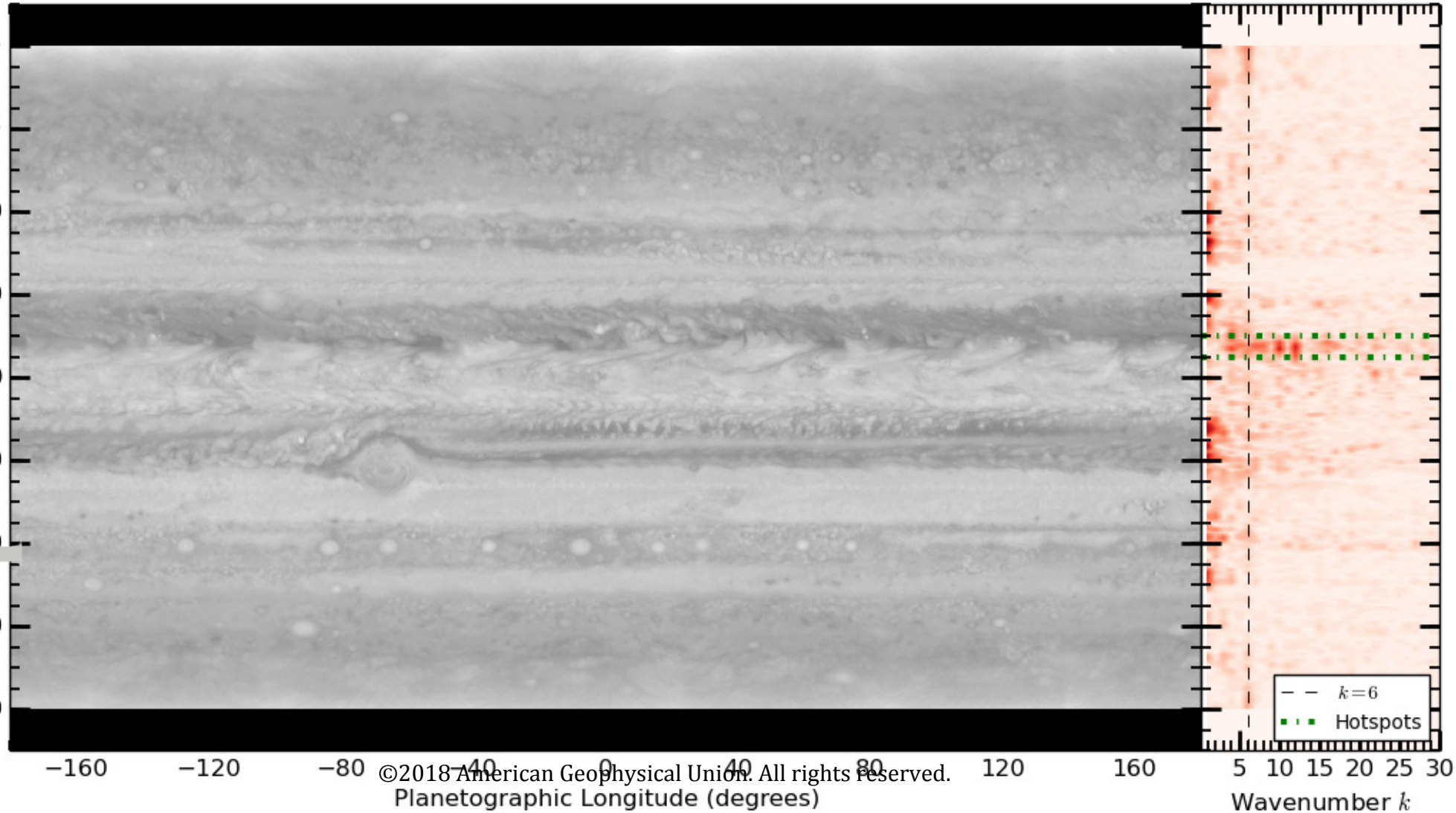

Figure 2.

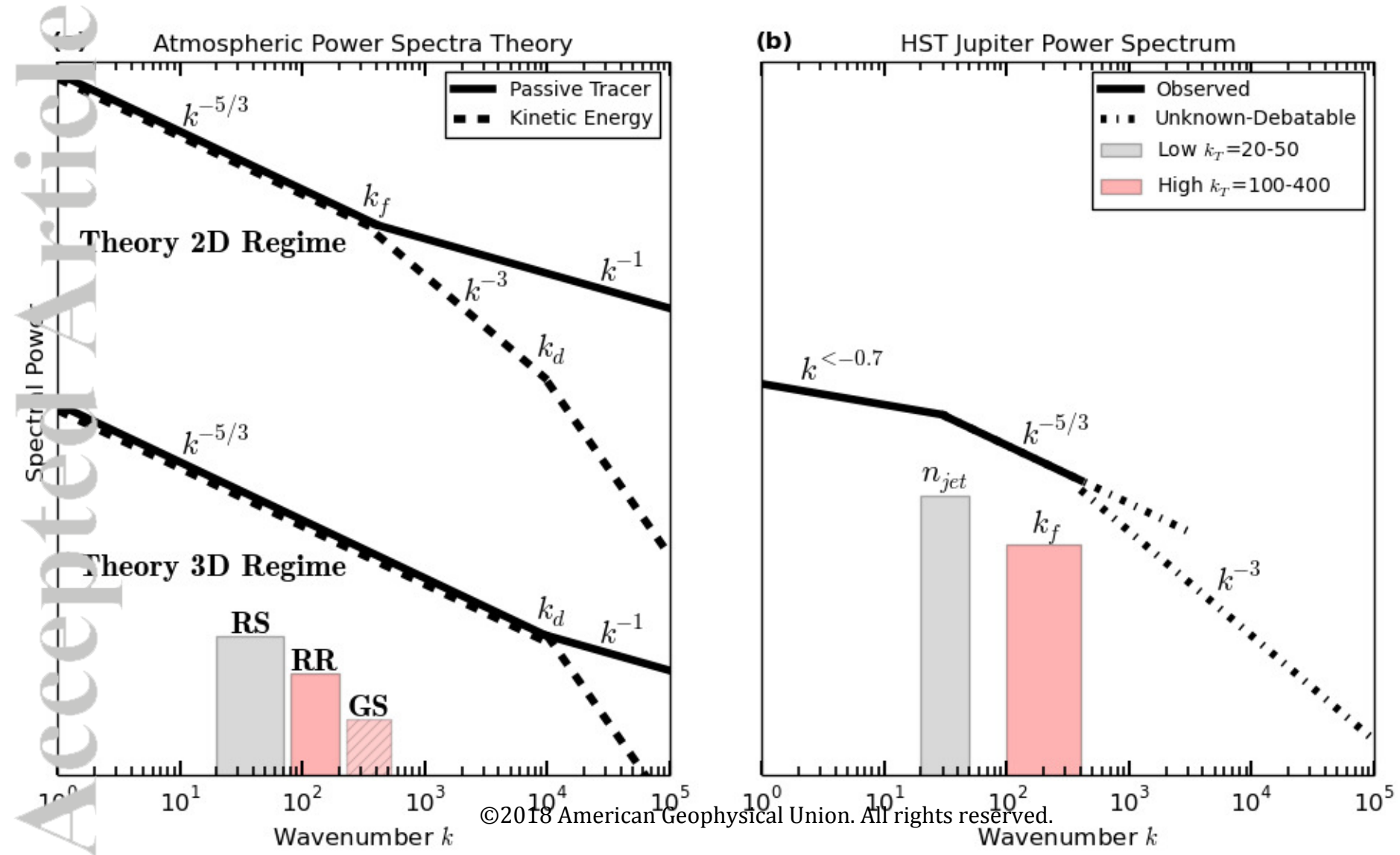

Figure 3.

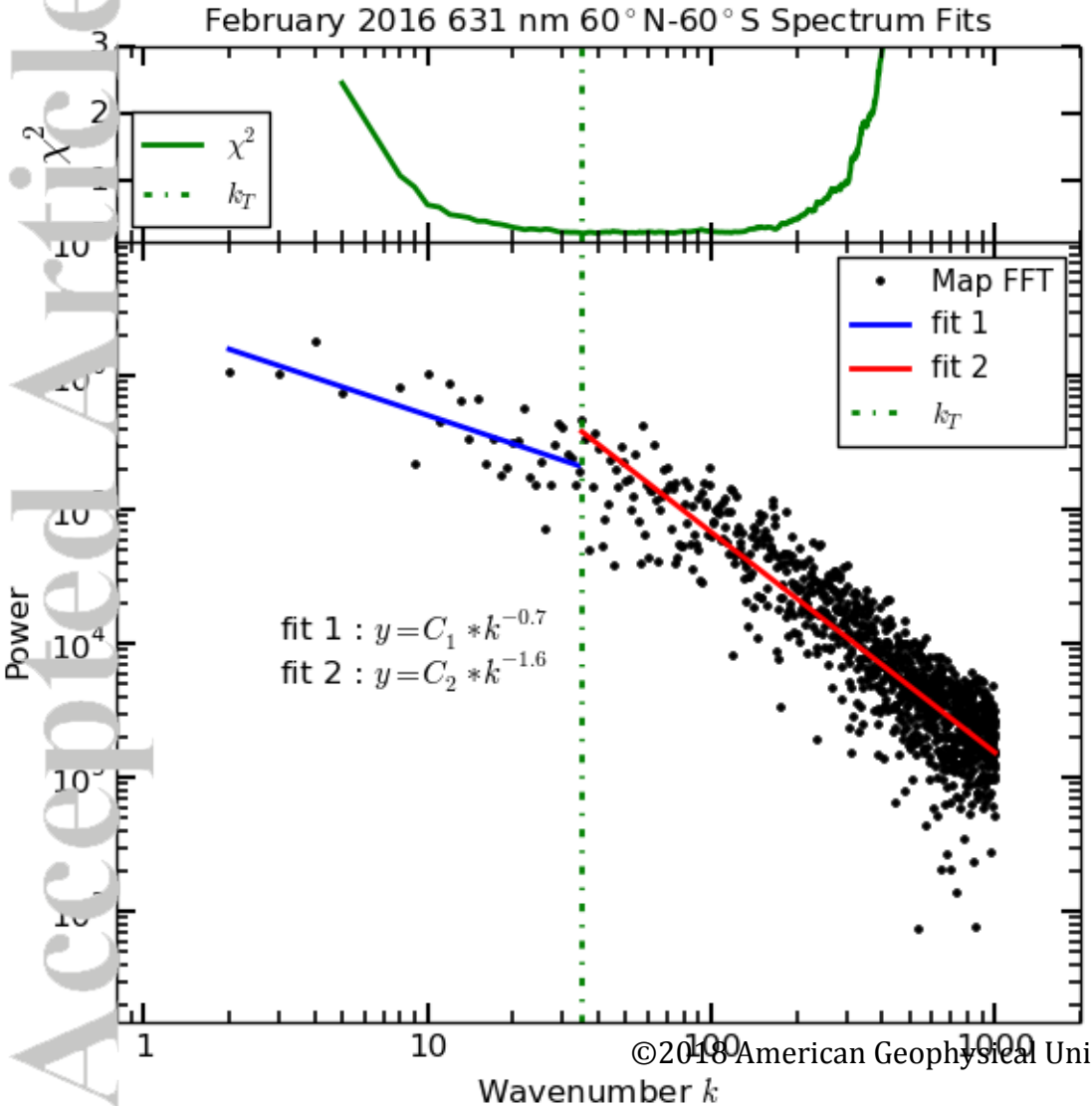

Figure 4.

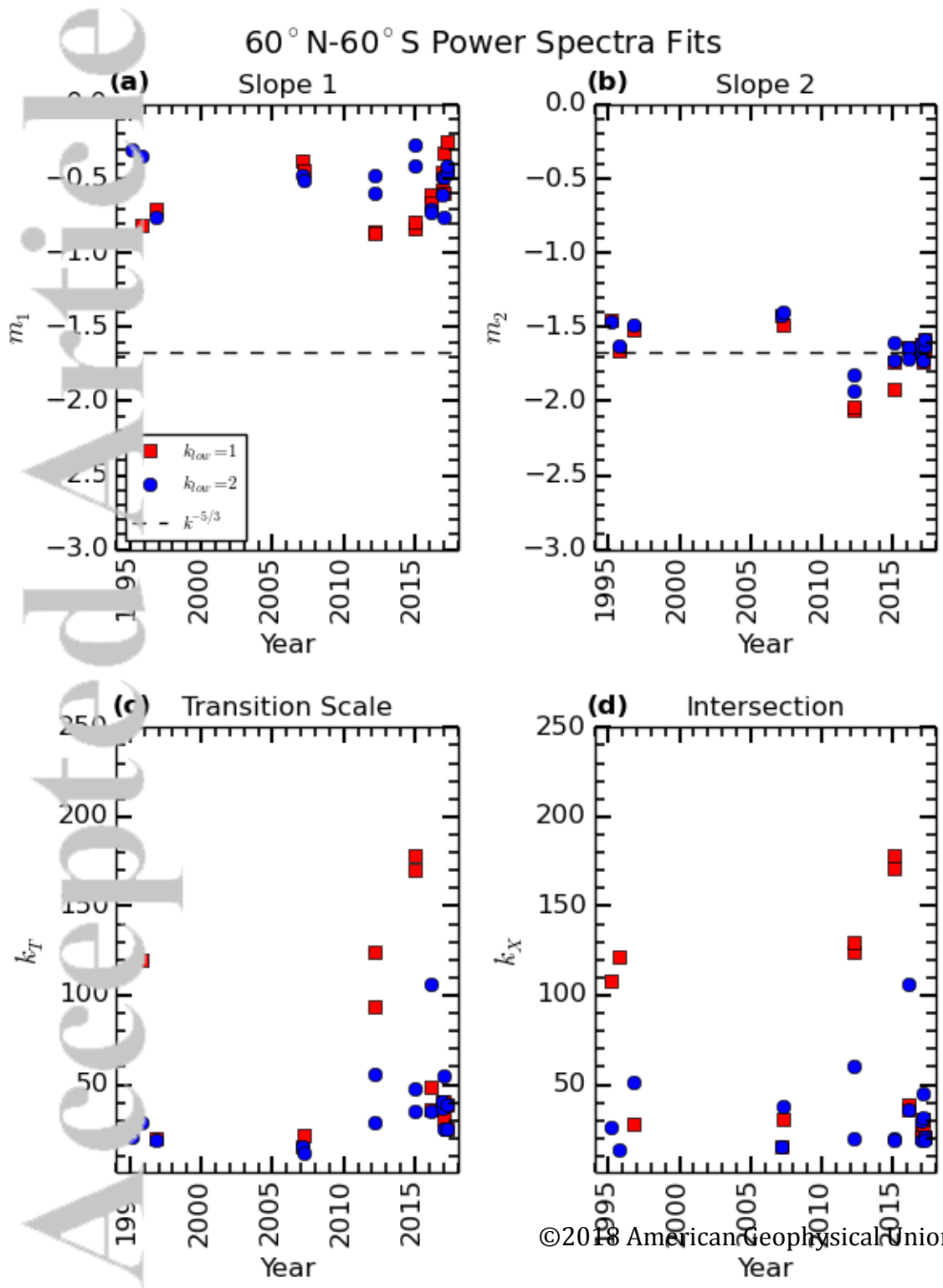

Figure 5.

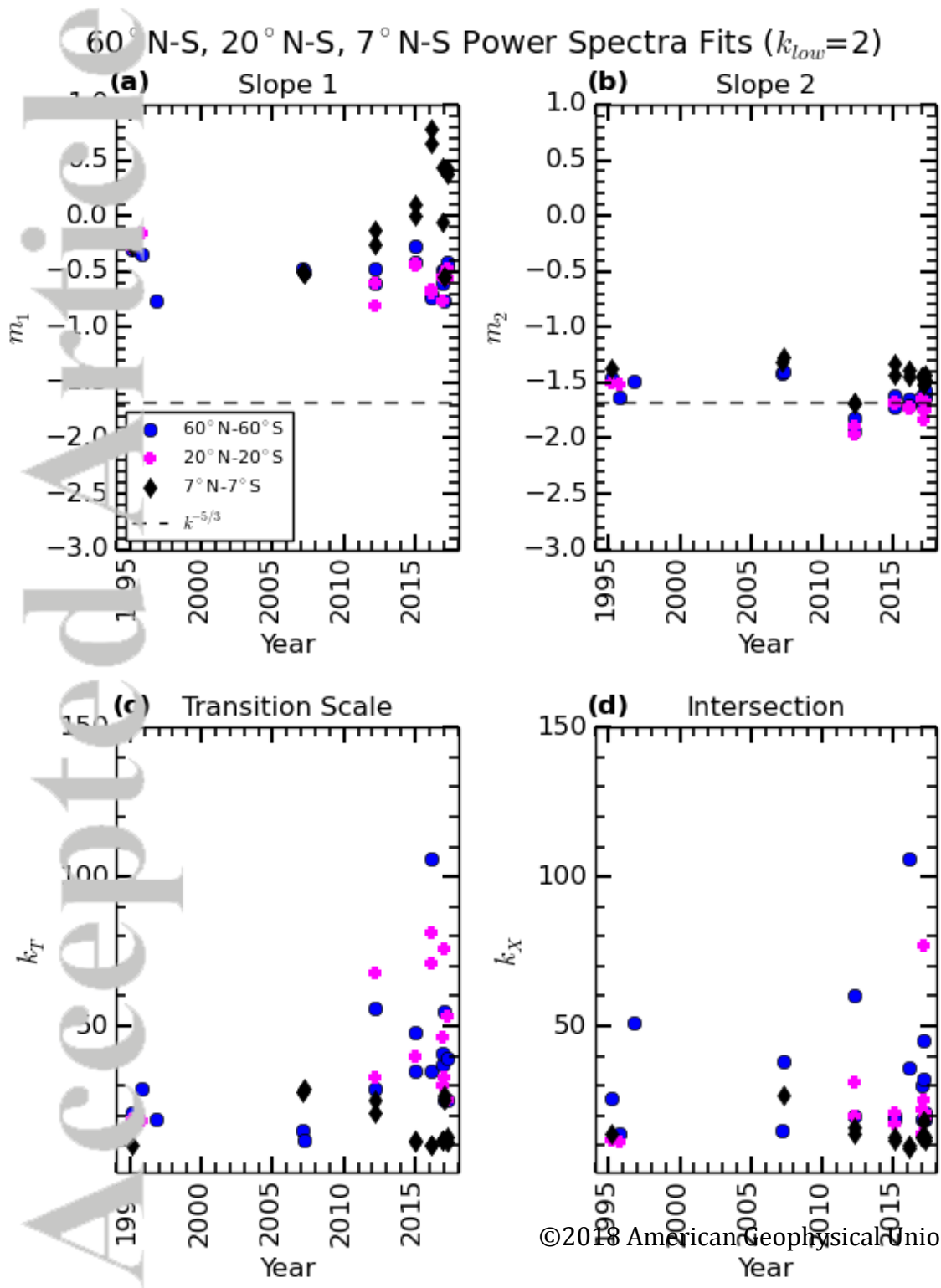

Figure 6.

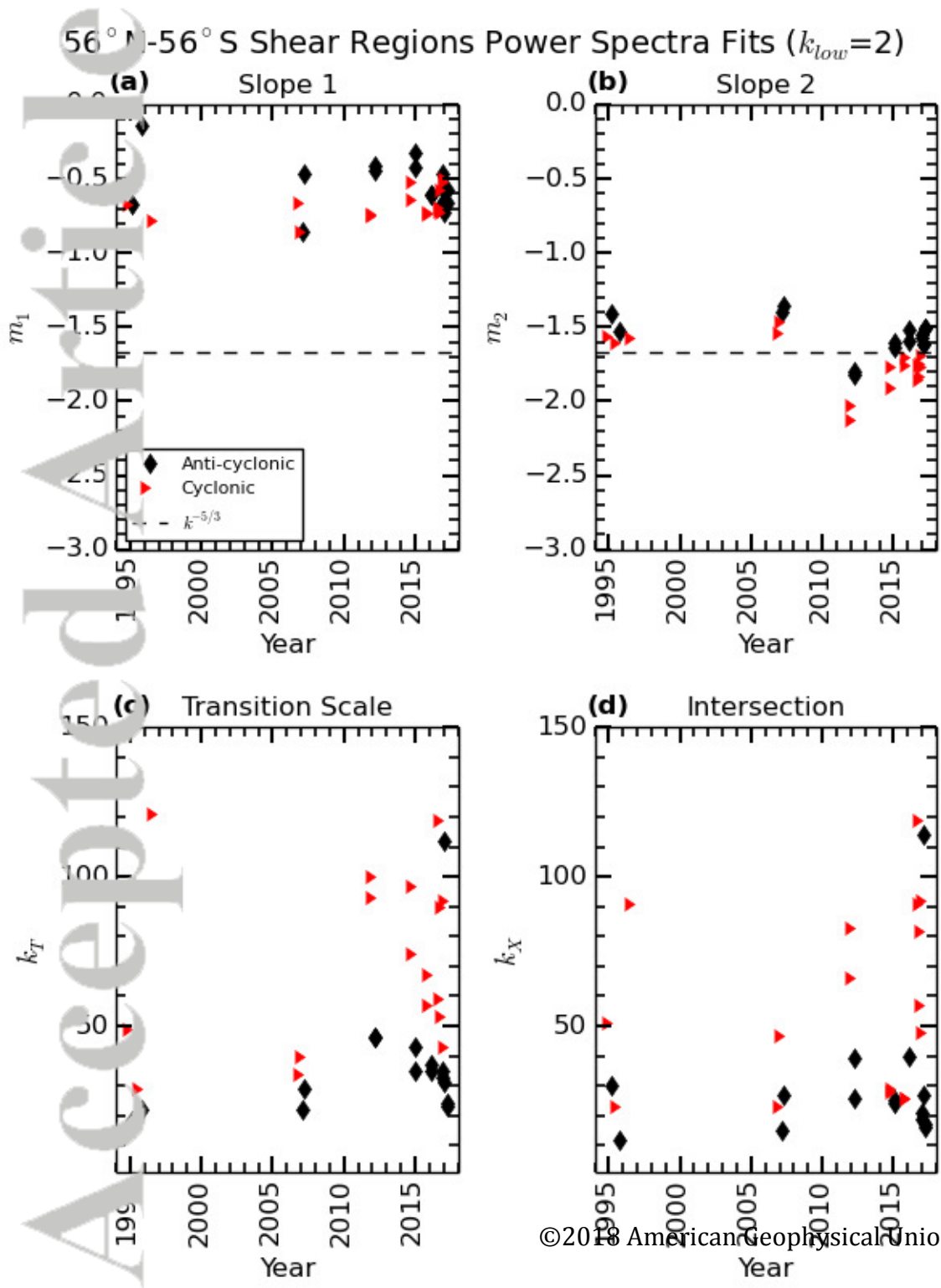

Figure 7.

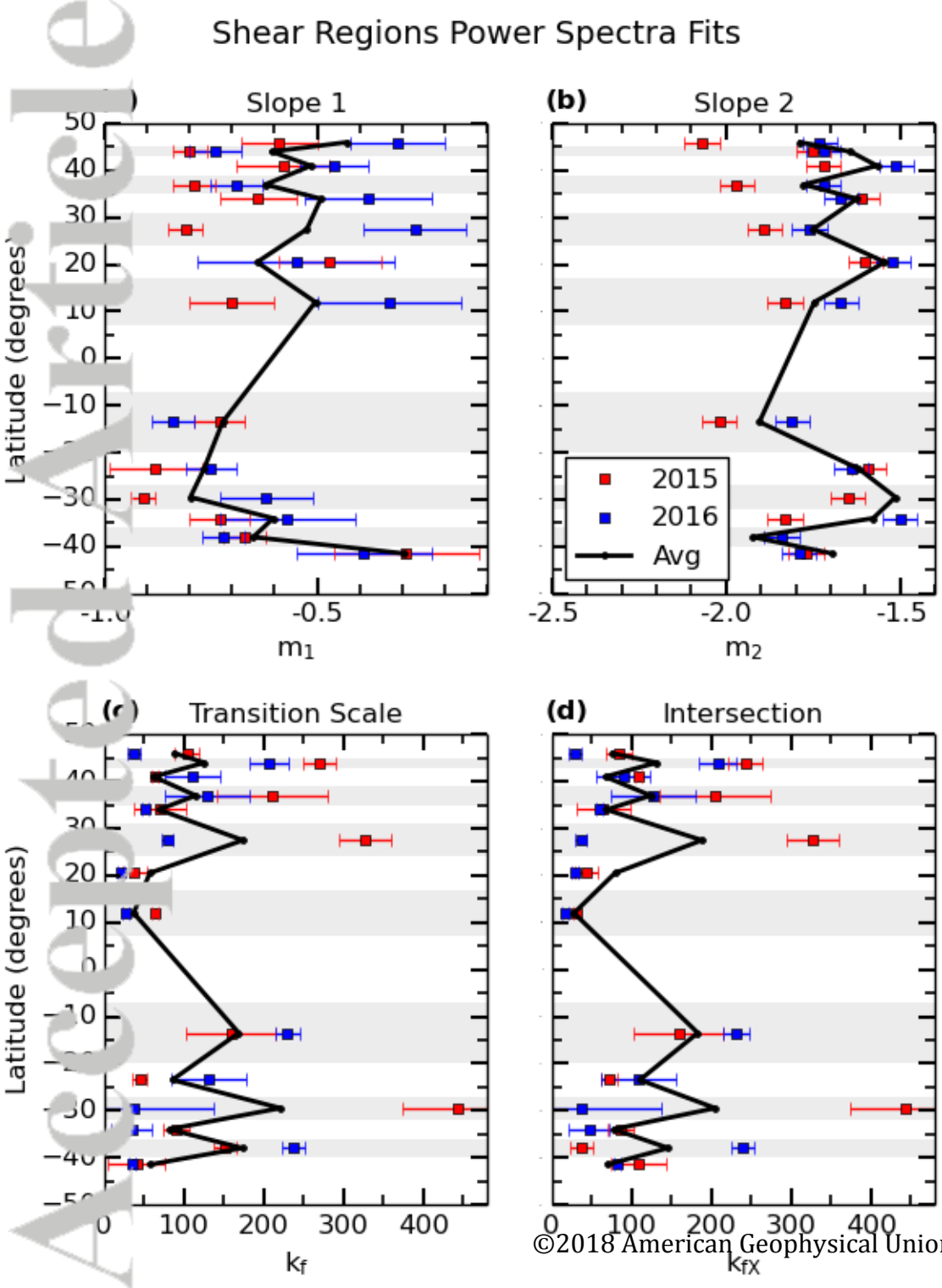

Figure A1.

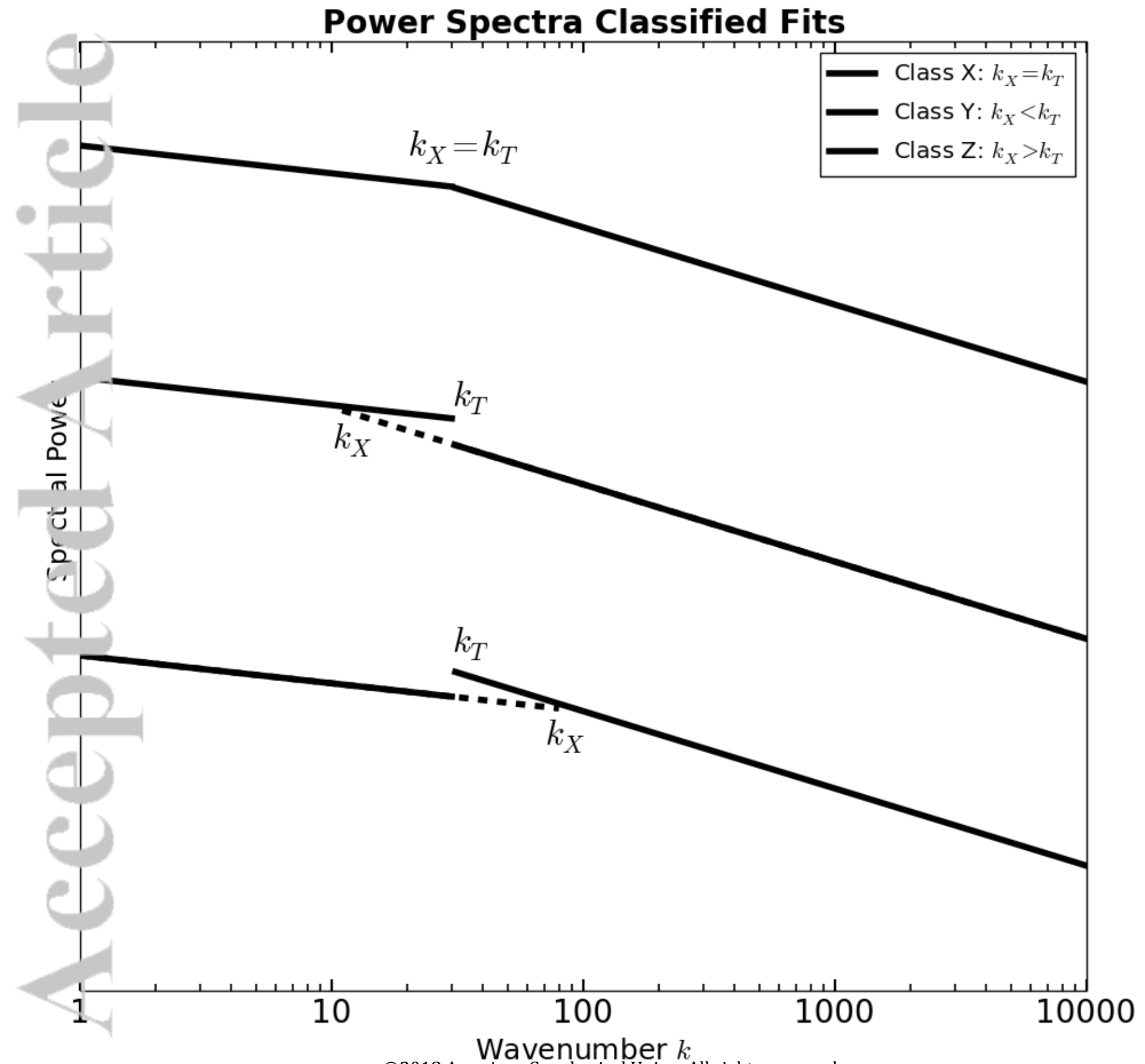

Figure A2.

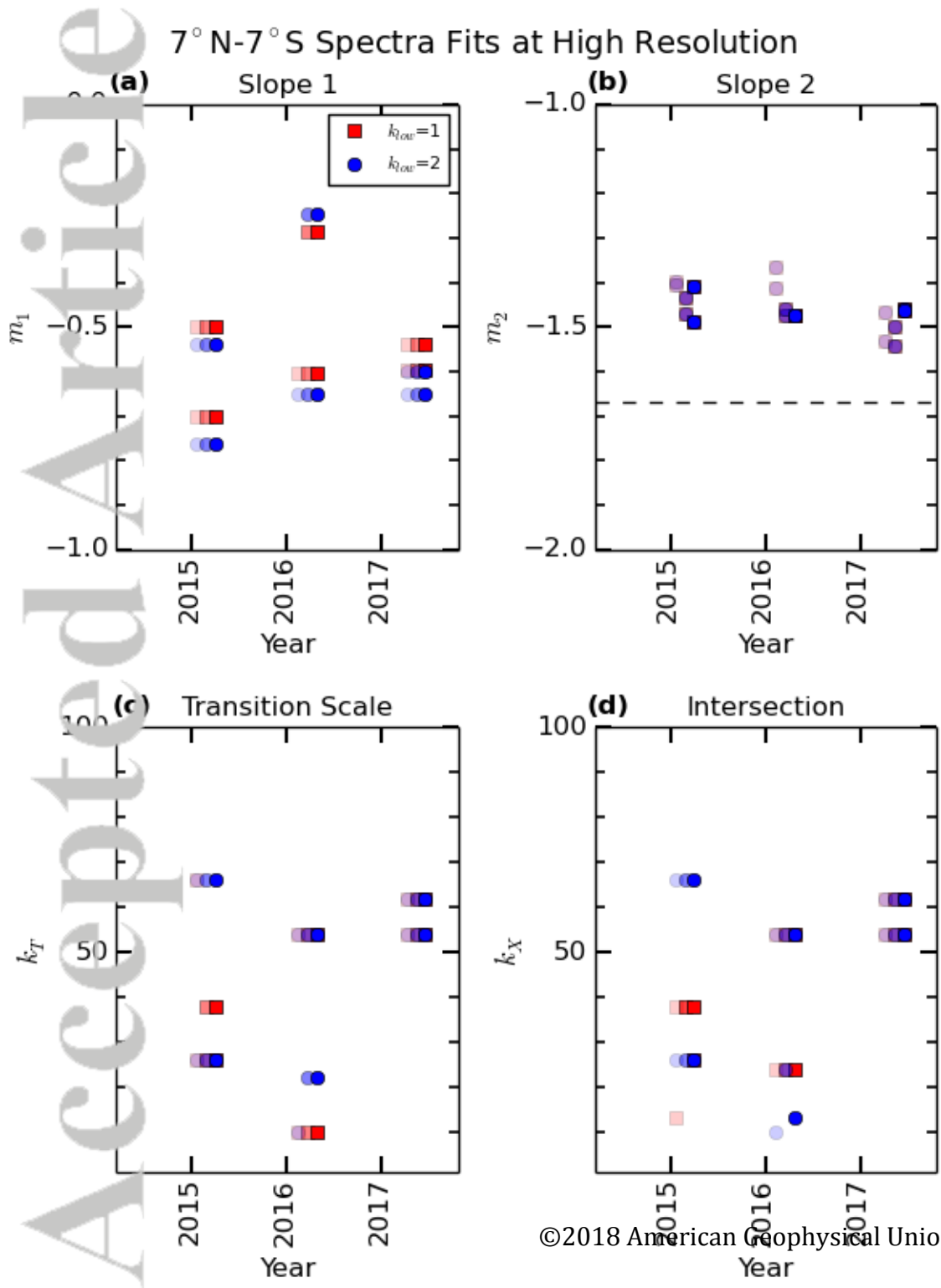

Figure A3.

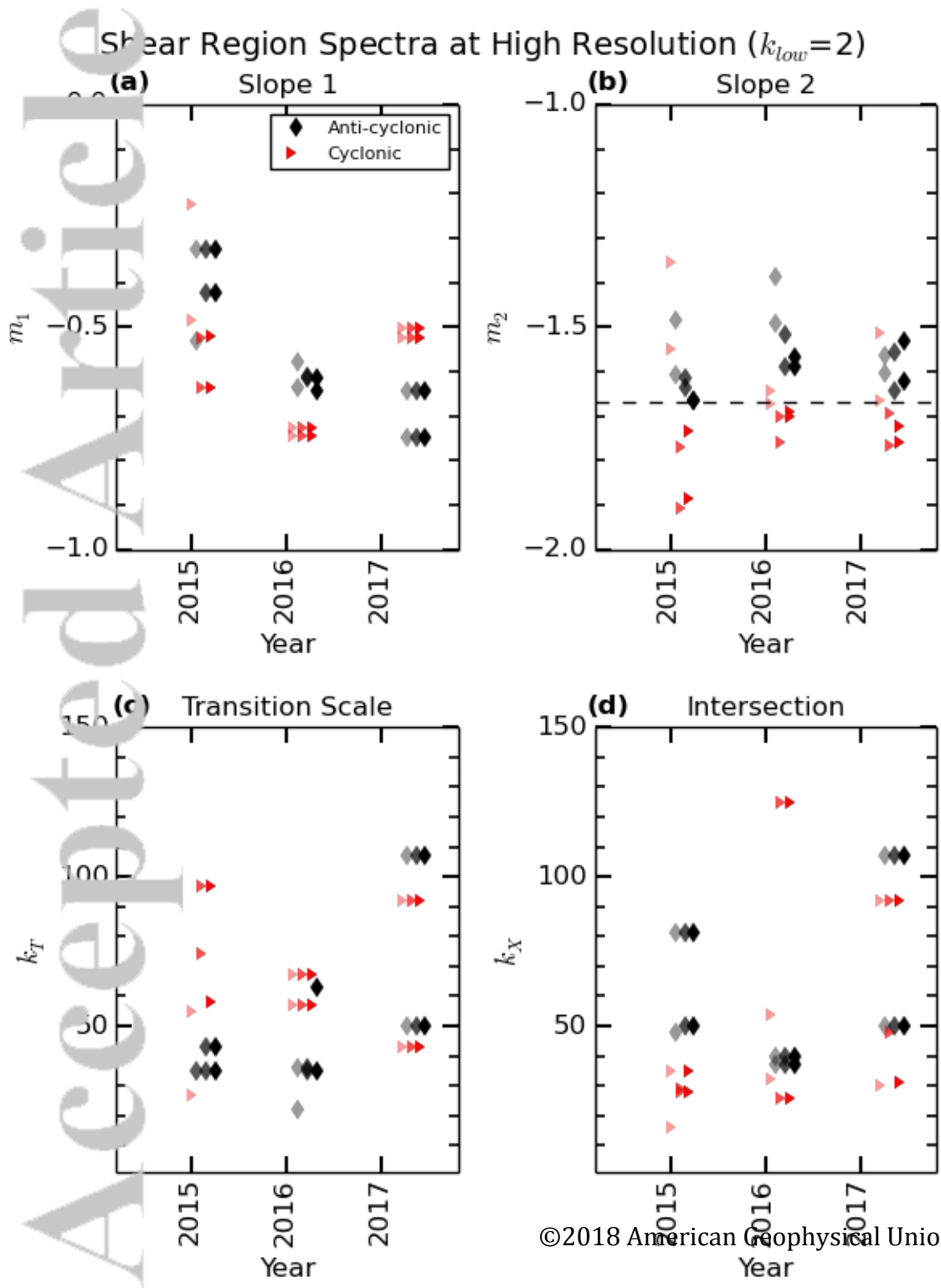

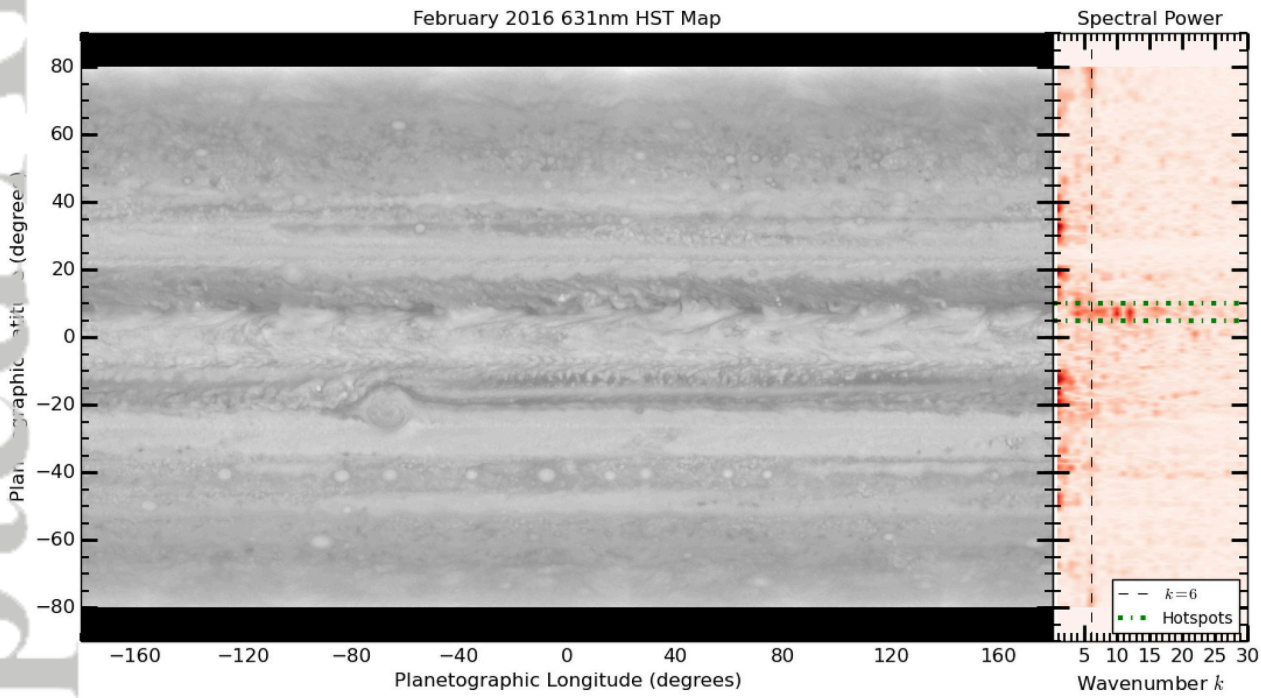

2018je005762-t-f01-z-.eps

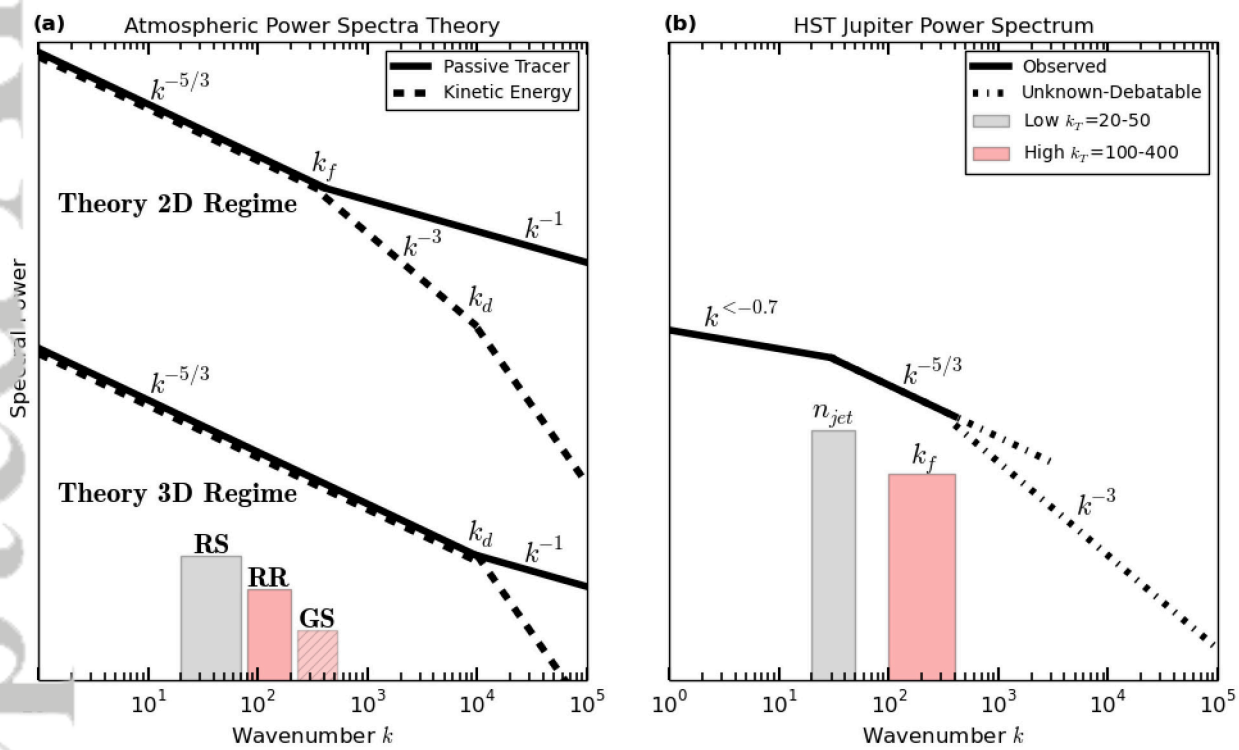

2018je005762-t-f02-z-.eps

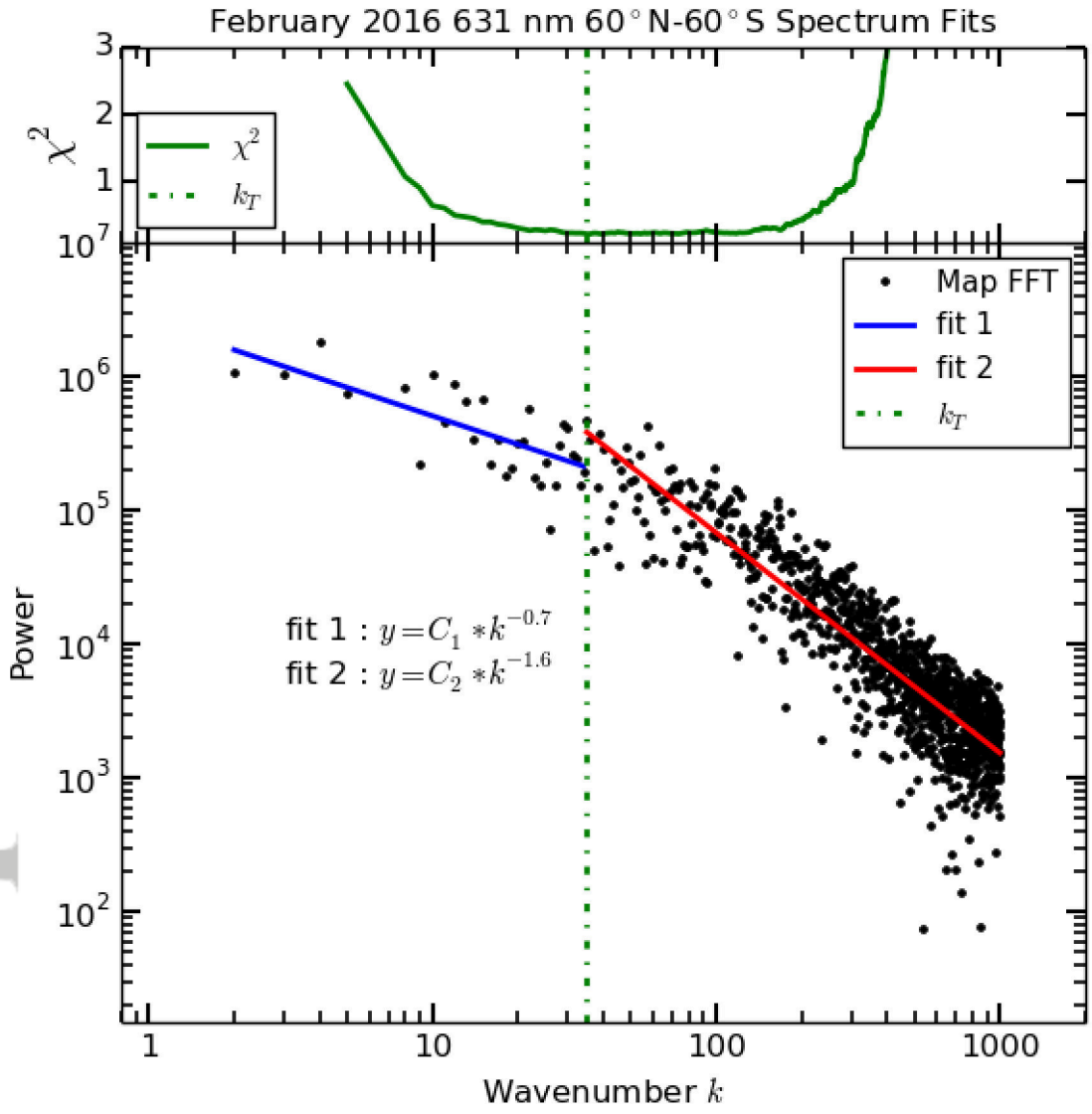

2018je005762-t-f03-z-.eps

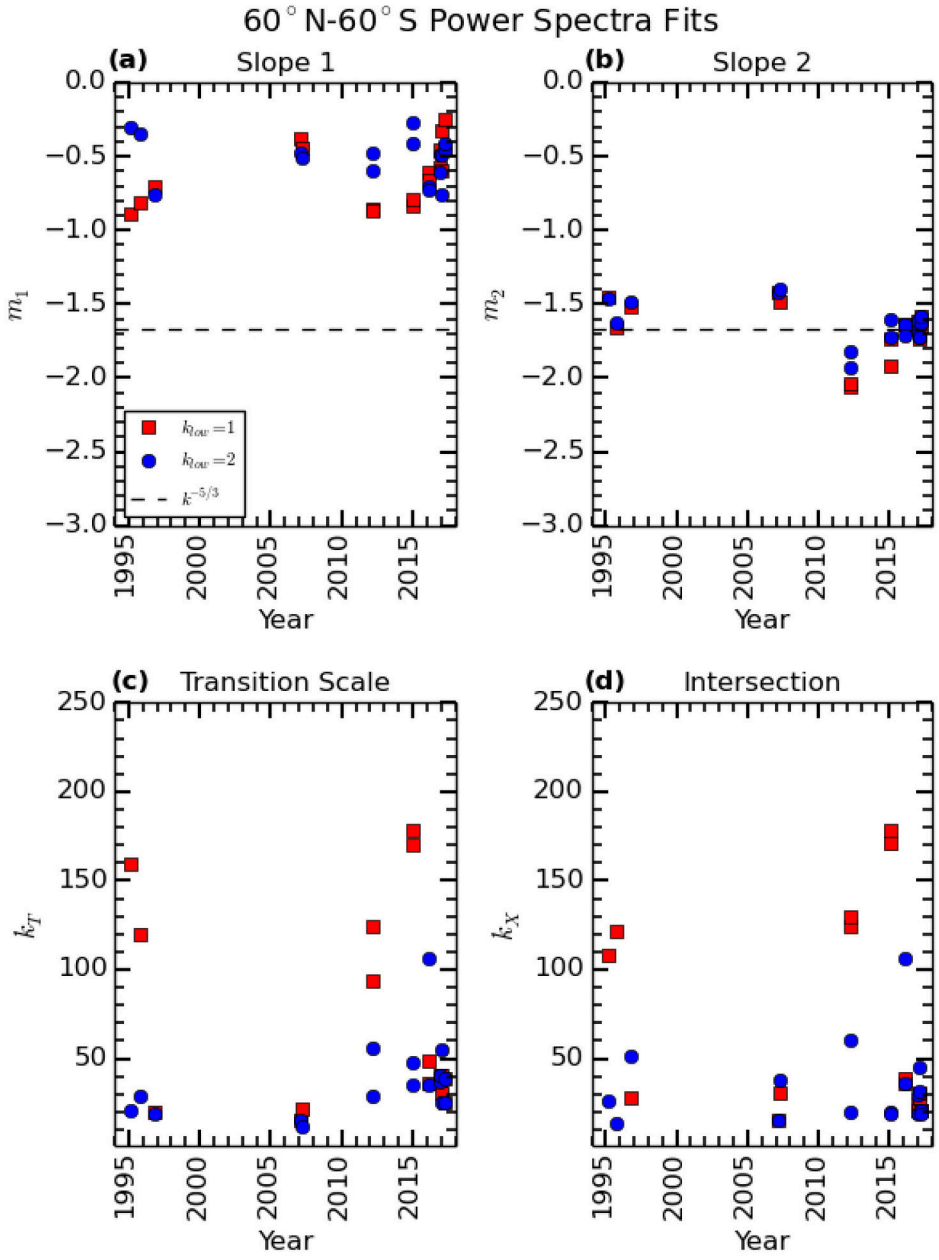

2018je005762-t-f04-z-.eps

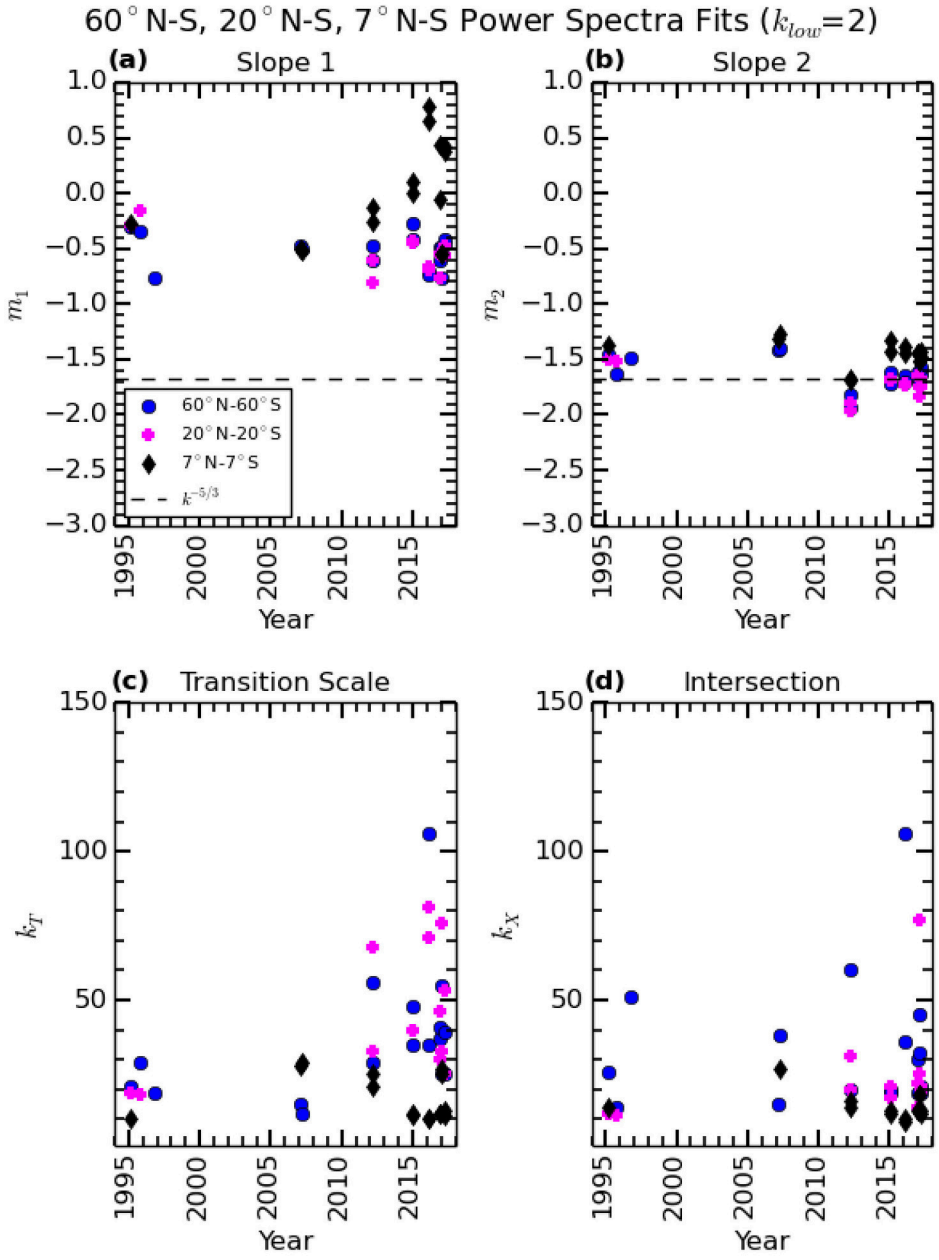

2018je005762-t-f05-z-.eps

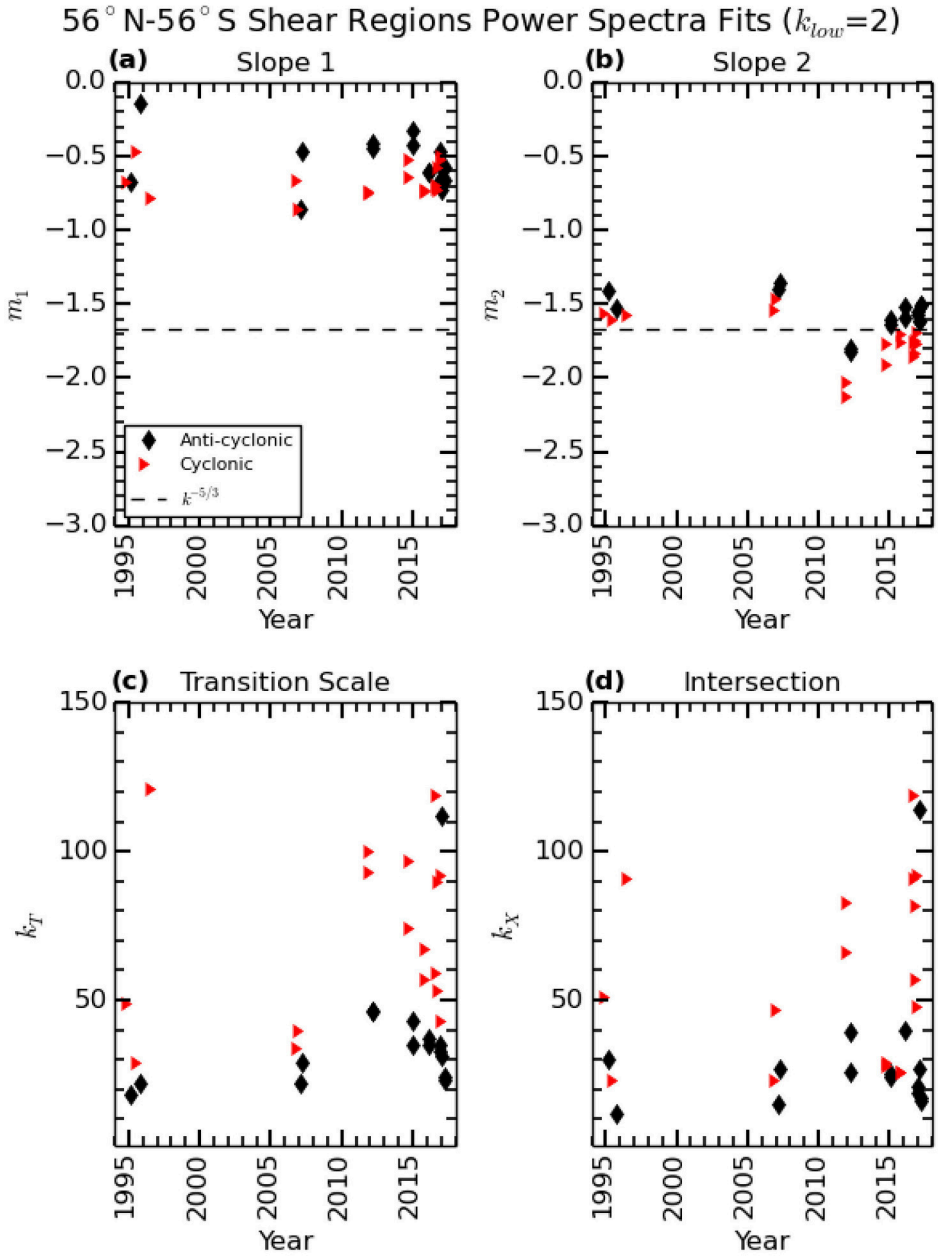

2018je005762-t-f06-z-.eps

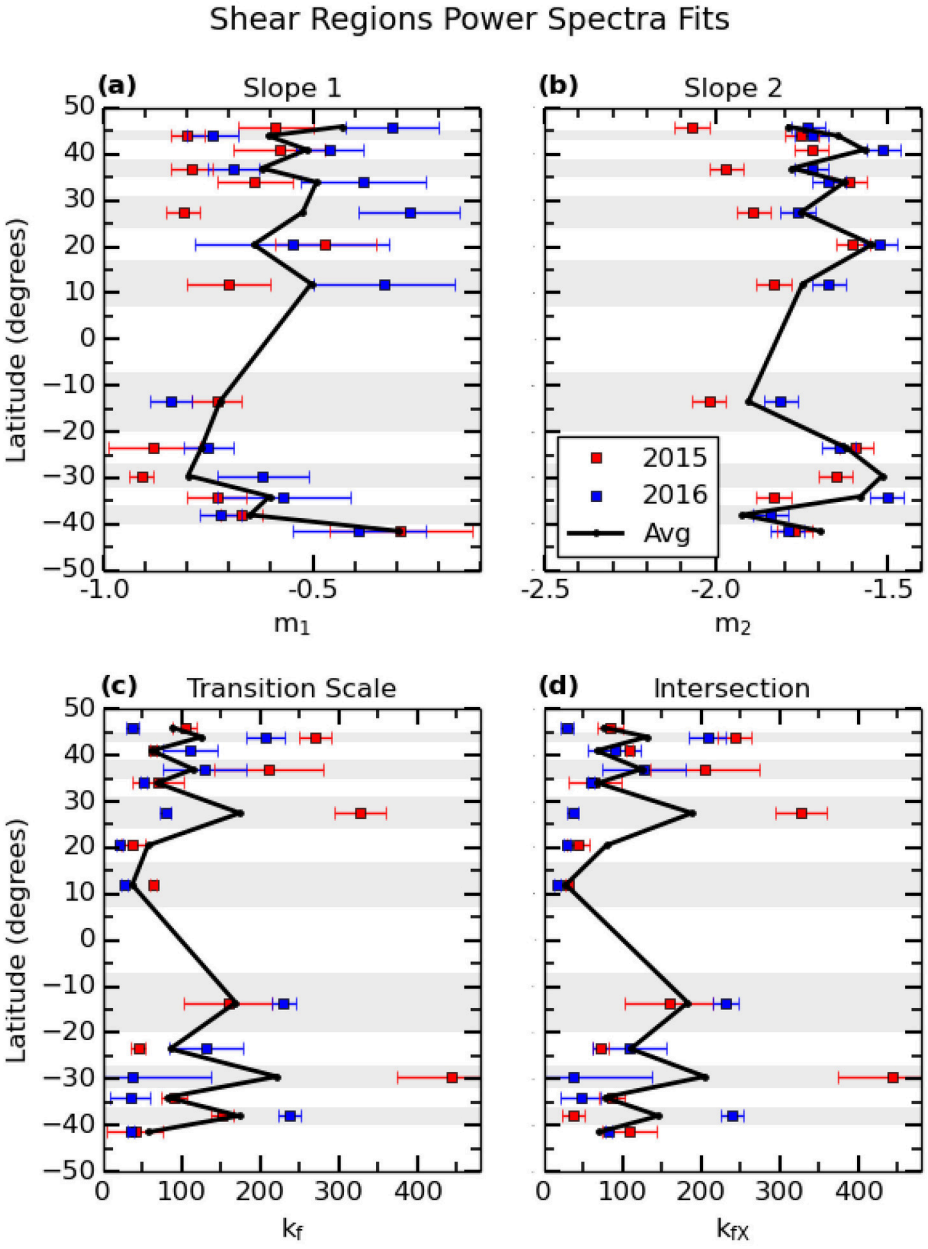

2018je005762-t-f07-z-.eps

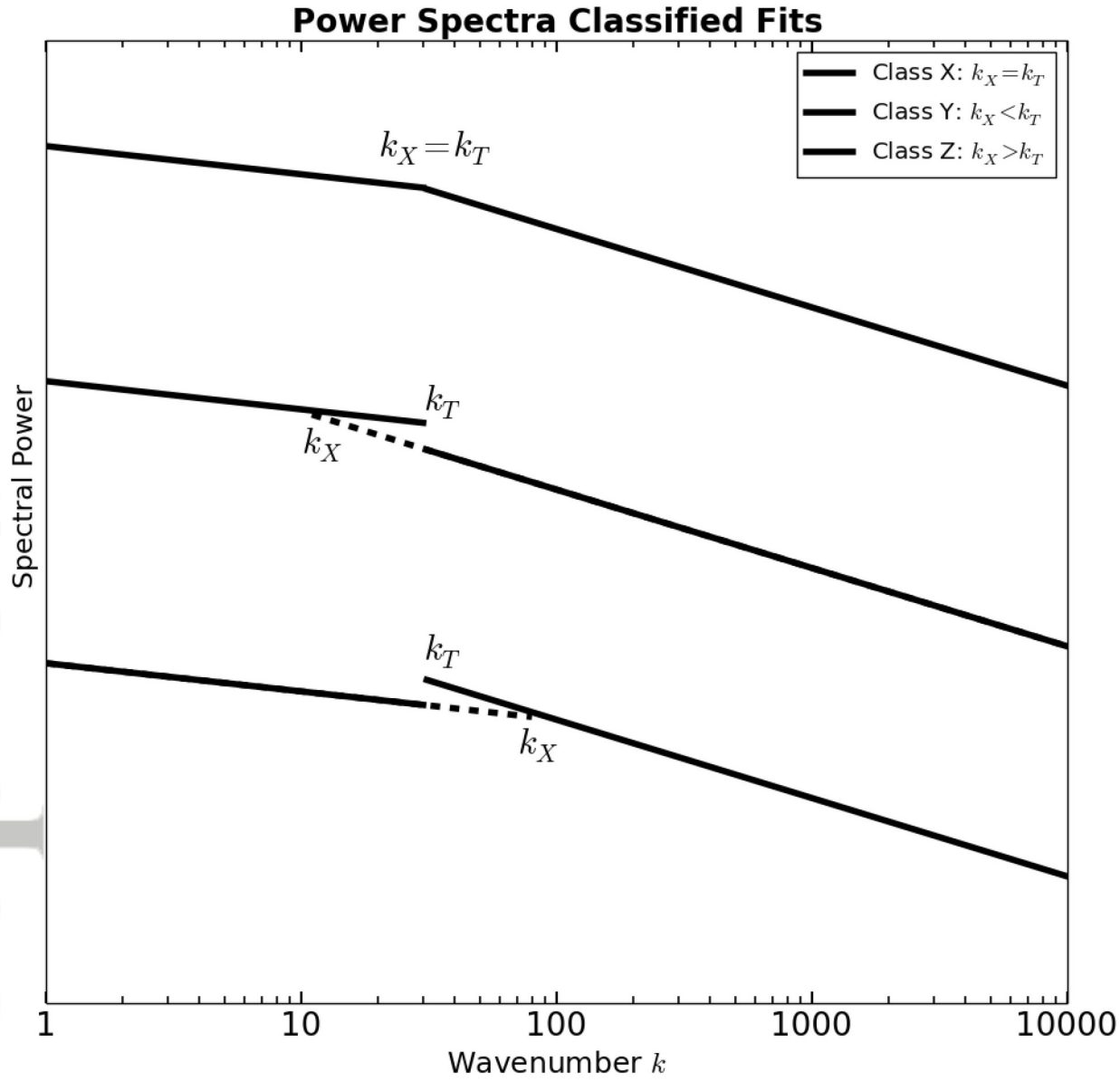

2018je005762-t-f08-z-.eps

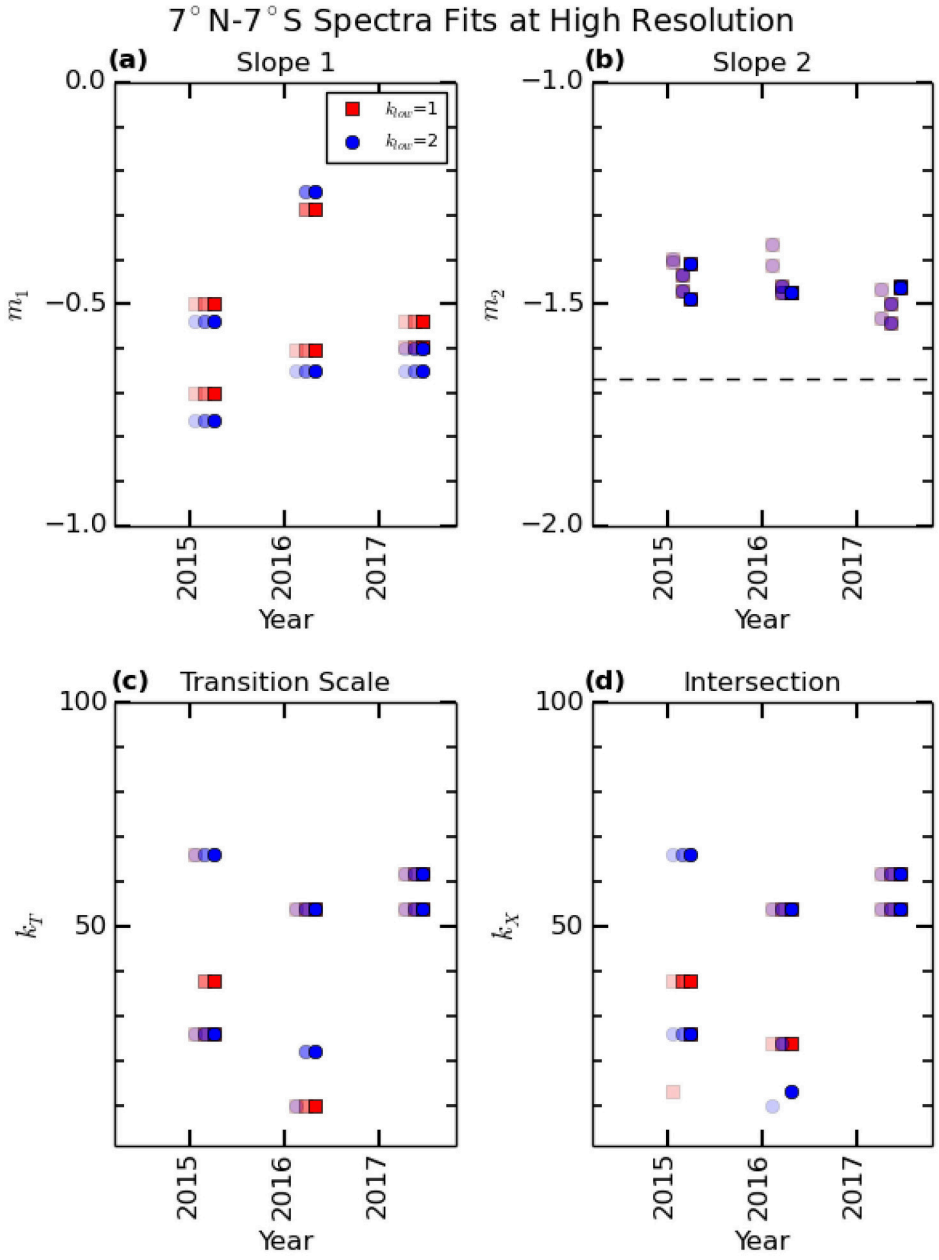

2018je005762-t-f09-z-.eps

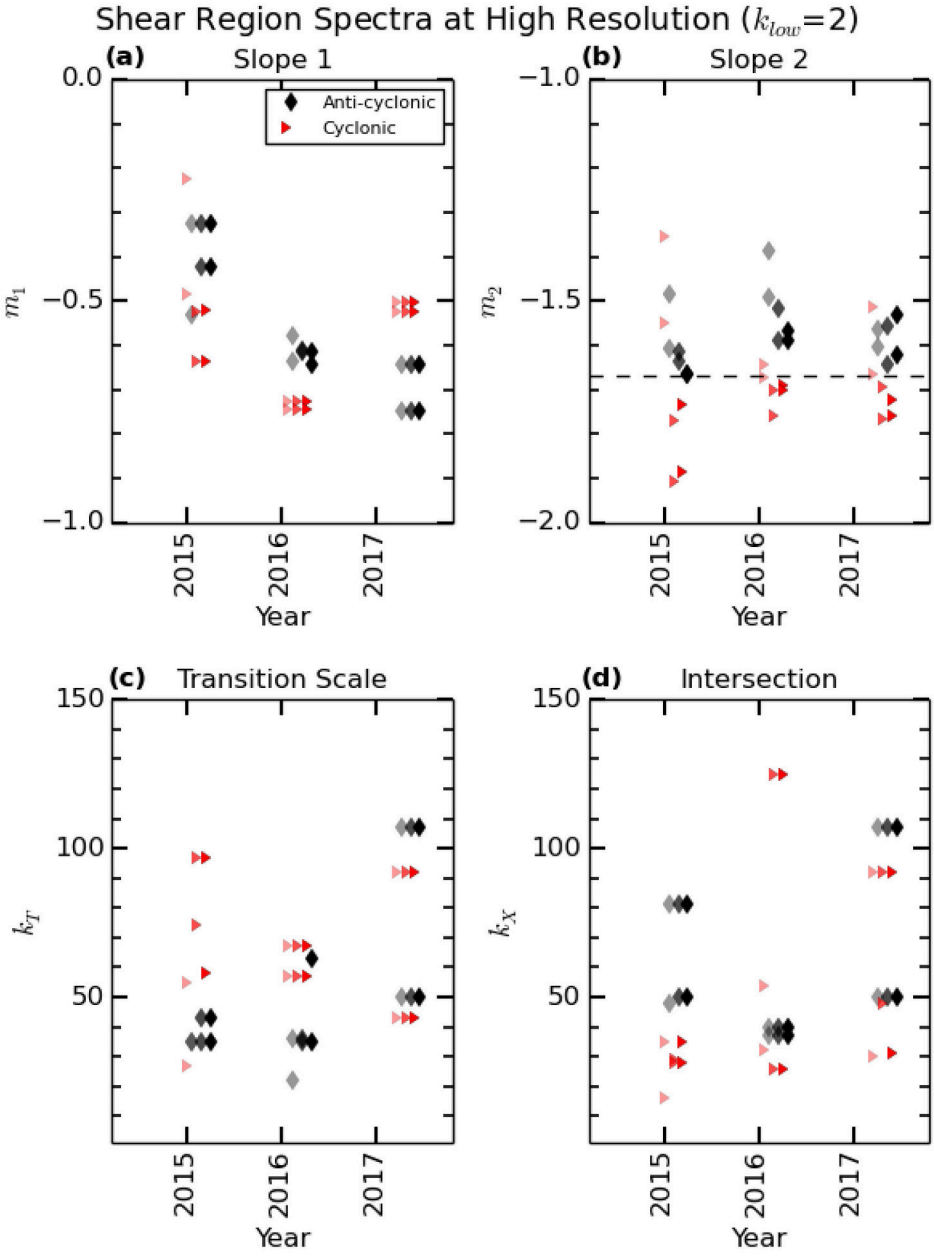

2018je005762-t-f10-z-.eps